Wideband Beamforming for Hybrid Massive MIMO Terahertz Communications

Feifei Gao, *Fellow, IEEE*, Bolei Wang, *Member, IEEE*, Chengwen Xing, *Member, IEEE*, Jianping An, *Member, IEEE*, and Geoffrey Ye Li, *Fellow, IEEE*

***Abstract*—The combination of large bandwidth at terahertz (THz) and the large number of antennas in massive MIMO results in the non-negligible spatial wideband effect in time domain or the corresponding beam squint issue in frequency domain, which will cause severe performance degradation if not properly treated. In particular, for a phased array based hybrid transceiver, there exists a contradiction between the requirement of mitigating the beam squint issue and the hardware implementation of the analog beamformer/combiner, which makes the accurate beamforming an enormous challenge. In this paper, we propose two wideband hybrid beamforming approaches, based on the virtual sub-array and the true-time-delay (TTD) lines, respectively, to eliminate the impact of beam squint. The former one divides the whole array into several virtual sub-arrays to generate a wider beam and provides an evenly distributed array gain across the whole operating frequency band. To further enhance the beamforming performance and thoroughly address the aforementioned contradiction, the latter one introduces the TTD lines and propose a new hardware implementation of analog beamformer/combiner. This TTD-aided hybrid implementation enables the wideband beamforming and achieves the near-optimal performance close to full-digital transceivers. Analytical and numerical results demonstrate the effectiveness of two proposed wideband beamforming approaches.**

***Index Terms*—Wideband beamforming, hybrid, THz, beam squint, virtual sub-array, true-time-delay.**

I. Introduction

Terahertz (THz) communications are promising for the fifth generation (5G) and beyond 5G wireless communication networks [1]–[3]. In World Radiocommunication Conference 2019 (WRC-19), the frequency bands 275-296 GHz, 306-313 GHz, 318-333 GHz, and 356-450 GHz have been identified for land mobile and fixed service applications [4]. The abundant THz spectrum resource (0.1–10 THz) is able to offer unprecedented tens of gigahertz (GHz) bandwidth, achieve even several Tbps of data transmission rates [5], and accommodate tremendous numbers of devices simultaneously.

To deal with the severe path loss in THz band, massive multiple-input multiple-output (MIMO) technology is the key enabler [5]. Furthermore, the extremely short wavelength in THz enables the concept of ultra-massive MIMO [6], [7], which embeds thousands of antennas in a few square millimeters. Therefore, accurate beamforming with massive MIMO is crucial to guarantee the enough signal-to-noise ratio (SNR) and thereby obtain the benefit from THz frequency band. Different from the sub-6 GHz frequency band where the full-digital transceivers are achievable, in the high frequency band, such as millimeter-wave (mmWave) and THz, the full-digital architecture becomes impractical due to the unaffordable hardware cost, power consumption, and difficulty of hardware integration [8], [9]. In this case, the hybrid analog and digital precoding/combining has emerged as the dominant architecture to tradeoff performance and cost [10]–[13]. The hybrid architecture lowers the cost by largely reducing the number of RF chains and transferring some signal processing task from the digital baseband signal processor to the analog beamformer/combiner, which, however, introduces additional constraints that highly limits the beamforming ability. Various precoding algorithms for full-digital architectures need to be revised or redesigned for hybrid transceivers. In [14], the performance of beamforming and that of multiplexing at THz band are compared to demonstrate the importance of accurate beamforming in the relatively longer distance transmission, say beyond a few meters such as 10 meters. Several hybrid beamforming techniques in [15]–[19] focus on the narrowband case. To address the limitation of the narrowband transmission, a few wideband hybrid precoding techniques have been developed in [20]–[23]. The hybrid precoding method in [20] considers rate and coverage constraint for wideband massive MIMO-OFDM system. The hybrid precoding method in [21] exploits sparse optimization for single-carrier wideband systems. In [22], the analog beamforming is based on beam-steering codebook while the digital beamforming uses the regularized channel inversion method for wideband beamforming over frequency selective channels. The distance-aware adaptive beamforming and resource allocation are jointly considered for indoor THz communications in [23]. However, these precoding techniques ignores the beam squint issue [24], which may cause severe beamforming performance degradation if not property treated.

Actually, the combination of the large bandwidth and the large number of antennas results in the non-negligible propagation delay across the antenna array aperture in time-domain sample periods, which is called spatial wideband effect [25], [26] and causes beam squint in frequency domain [24]. Basically, for an incident path, beam squint makes different frequencies to observe distinct angles in a large array if the same steering vector is adopted as the combiner for different frequencies. Conversely, if the same steering vector is employed for different frequencies in beamforming

F. Gao and B. Wang are with Institute for Artificial Intelligence, Tsinghua University (THUAI), State Key Lab of Intelligent Technology and Systems, Tsinghua University, Beijing National Research Center for Information Science and Technology (BNRist), and Department of Automation, Tsinghua University, Beijing, China (e-mail: feifeigao@ieee.org; boleiwang@ieee.org).

C. Xing and J. An are with the School of Information and Electronics, Beijing Institute of Technology, Beijing 100081, China (e-mail: chengwenxing@ieee.org; an@bit.edu.cn).

G. Y. Li is with the Department of Electrical and Electronic Engineering, Imperial College London, London, UK (email: Geoffrey.Li@imperial.ac.uk).

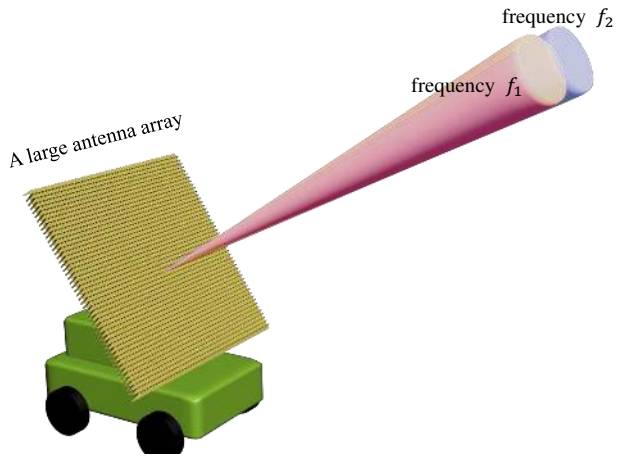

Fig. 1. Beam squint effect in a large antenna array.

or precoding, a transmitter will generate dispersed beam such that the signals at different frequencies point towards different physical directions, as illustrated in Fig. 1. As a result, the beamforming accuracy and directivity would deteriorate and the system capacity become limited in a wideband THz system with massive MIMO.

For a full-digital transceiver, the beam squint issue can be resolved by deploying different steering vectors for beamforming/combining at different frequencies. However, as will be discussed in Section III, for a hybrid phased array transceiver, beam squint is hard to be mitigated due to the hardware limitation of phase shifters. In fact, the phase shifters are essentially the narrowband devices such that a phased array can only generate the same steering vector over the whole frequency band. This incompatibility induces the contradiction between the requirement on mitigating the beam squint issue and the hardware implementation of the analog beamformer/combiner.

There exists some literature referring to the beam squint issue in hybrid precoding. The impact of beam squint on the random spatial sampling algorithm has been mentioned [27], which left its solution as future work, and has been considered in simulation in [28], which have found that beam squint causes the degradation of average spectral efficiency. The precoding design in [24] has used several RF chains to generate frequency-dependent steering vectors, partially alleviating the impact of beam squint but inducing the high hardware cost.

Large phased arrays were initially invented for military radar systems, where large bandwidth is also required to achieve high spatial resolution for target recognition [31]. Consequently, radars naturally tend to have large arrays and large bandwidth, which, however, cause the considerable effect of beam squint that largely limits the beamforming performance. Therefore, beam squint has been initially investigated in radar systems [29], [30]. A general solution to this issue for radar systems is employing the true-time-delay (TTD) lines to replace phase shifters [32]–[34]. The impact of beam squint on radiation patterns and the necessity of the TTD lines for wideband phased array antennas have been shown in [32]. Different from a phase shifter that generates a fixed phase over the whole frequency band, a TTD line provides a programmable true time delay that induces the varying phase over frequencies. This feature of TTD lines can perfectly mitigate beam squint. However, it is impractical to substitute the TTD lines for all phase shifters since the TTD lines in higher frequency bands have larger hardware cost and power consumption, especially at THz band.

In this paper, we propose two wideband hybrid beamforming approaches, based on the virtual sub-array and the TTD lines, respectively, to eliminate the impact of beam squint. The former one designs analog beamforming by dividing the whole array into several virtual sub-arrays to generate a beam with evenly distributed array gain across the whole frequency band. The latter one introduces the TTD lines and redesigns the analog beamformer/combiner for a hybrid phased array transceiver. By providing additional delays for different antennas in time domain to alleviate the spatial wideband effect, which is the essence of beam squint, the TTD lines enable the wideband beamforming of analog part in hybrid transceivers and the TTD-aided hybrid beamforming achieves the near-optimal performance close to the full-digital transceivers. Different from the typical TTD beamsteering architecture in wideband radars [35], where all phase shifters are replaced with TTD lines, the proposed TTD-based architecture only uses a few TTD lines and is an economical implementation, where the TTD lines are much fewer than the phase shifters but enough to effectively eliminate the impact of beam squint.

The rest of this paper is organized as follows. Section II introduces the hybrid channel model with beam squint. Section III reveals the incompatibility and the corresponding contradiction between the requirement on mitigating the beam squint issue and the hardware implementation of the analog beamformer/combiner. Section IV proposes a virtual sub-array based analog beamforming technique with beam broadening and the corresponding hybrid beamforming approach. Section V discusses the TTD-based analog beamforming and designs the corresponding hybrid beamforming approach. The simulation results are shown in Section VI to demonstrate the effectiveness of the proposed approaches. Section VII concludes this paper.

Notations: Uppercase boldface and lowercase boldface denote matrices and vectors, respectively. Superscripts $(\cdot)^T, (\cdot)^H, (\cdot)^*, (\cdot)^\dagger$ stand for the transpose, the conjugate-transpose, the conjugate, and the pseudo-inversion of a matrix or a vector, respectively. Symbols $\mathbf{I}$, $\mathbf{1}$, and $\mathbf{0}$ represent the identity matrix, the all-ones matrix, and the all-zeros matrix, respectively, while their subscripts, if needed, indicate the dimensionality. Symbols $\odot$ and $\otimes$ denote the Hadamard product and the Kronecker product of two matrices, respectively. $\mathbb{E}\{\cdot\}$ denotes the expectation. $\|\mathbf{a}\|_2$ and $\|\mathbf{A}\|_F$ denote the Euclidean norm of vector $\mathbf{a}$ and the Frobenius norm of matrix $\mathbf{A}$, respectively. We use $[\mathbf{A}]_{m,n}$, $[\mathbf{A}]_{:,n}$, and $[\mathbf{A}]_{m,:}$ to denote the (m,n)th element, the nth column, and the mth row of matrix $\mathbf{A}$, respectively. We also employ $[\mathbf{A}]_{:,\mathcal{Q}}$, and $[\mathbf{A}]_{\mathcal{P},:}$ to represent the submatrices extracted from subset $\mathcal{Q}$ of the columns of matrix $\mathbf{A}$ and subset $\mathcal{P}$ of the rows of matrix $\mathbf{A}$, respectively. $\mathrm{diag}\{\mathbf{a}\}$ denotes the diagonal matrix

comprising vector $\mathbf{a}$'s elements and diag$\{\mathbf{A}\}$ represents the vector extracted from the diagonal entries of matrix $\mathbf{A}$. $|\mathcal{A}|$ is the cardinality of set $\mathcal{A}$. $\lceil x \rceil$ denotes the minimum integer that is not smaller than x, $\lceil x \rfloor$ denotes the integer nearest to x, and $\lfloor x \rfloor$ denotes the maximum integer that is not bigger than x.

II. System Model

We consider the downlink beamforming design for a wideband THz massive MIMO system with a base station (BS) and a served user. The BS is equipped with an M-antenna uniform linear array (ULA) and the served user has an M_U-antenna ULA. Both ULAs contain the identical and isotropic antennas with antenna spacing d. The transmission bandwidth and the carrier frequency are denoted as W and f_c, respectively.

Suppose that there are L incident paths from the user to the BS. We first consider the channel between *the first antenna of the user* and the mth antenna at the BS. Denote $\tau_{l,m}$ as the time delay of the lth path from the first antenna of the user to the mth antenna of the BS. Denote ϑ_l as the AoA of the lth path and define $\psi_l \triangleq \frac{d \sin \vartheta_l}{\lambda_c}$ as the normalized AoA, where c is the speed of light and $\lambda_c = c/f_c$ is the carrier wavelength.

Based on the far-field assumption that the size of the BS antenna array is much smaller than the distance between the user and the BS [36],

$$\tau_{l,m} = \tau_l + (m-1) \cdot \frac{d \sin \vartheta_l}{c} = \tau_l + (m-1) \cdot \frac{\psi_l}{f_c}, \quad (1)$$

where $\tau_l = \tau_{l,1}$ for notational simplicity. Considering the spatial-wideband effect [25], [26], the *time-domain* uplink channel between the first antenna of the user and the mth antenna of the BS can be expressed as

$$\begin{aligned} h_m(t) &= \sum_{l=1}^{L} \alpha_l e^{-j2\pi(m-1)\psi_l} \delta(t - \tau_{l,m}) \\ &= \sum_{l=1}^{L} \alpha_l e^{-j2\pi(m-1)\psi_l} \delta\Big(t - \tau_l - (m-1) \cdot \frac{\psi_l}{f_c}\Big), \end{aligned} \quad (2)$$

where α_l is the equivalent baseband complex gain of the lth path and $\delta(\cdot)$ denotes the Dirac delta function.

The spatial-wideband effect in time domain induces the *beam squint* effect in frequency domain [24], [26], as we can see subsequently. By taking the Fourier transform of (2), the corresponding frequency response of (2) can be obtain as

$$\begin{aligned} h_m^f(f) &= \sum_{l=1}^{L} \alpha_l e^{-j2\pi(m-1)\psi_l} e^{-j2\pi f \tau_{l,m}} \\ &= \sum_{l=1}^{L} \alpha_l e^{-j2\pi(m-1)\psi_l(1+\frac{f}{f_c})} e^{-j2\pi f \tau_l}, \end{aligned} \quad (3)$$

where $f \in [0, W]$ and the second equality utilizes the result in (1). Define

$$\Xi_l(f) \triangleq (1 + \frac{f}{f_c})\psi_l \quad (4)$$

and denote the steering vector as

$$\mathbf{a}(\psi) \triangleq [1, e^{-j2\pi\psi}, \ldots, e^{-j2\pi(M-1)\psi}]^T \in \mathbb{C}^{M \times 1}. \quad (5)$$

Stacking the channels of different antennas at given frequency f into a vector yields

$$\mathbf{h}(f) \triangleq \sum_{l=1}^{L} \alpha_l \mathbf{a}(\Xi_l(f)) e^{-j2\pi f \tau_l}, \quad (6)$$

where we can observe that the steering vector corresponding to each path becomes frequency-dependent, which is why it is called beam squint.

Denote $\vartheta_{U,l}$ as the angle of departure (AoD) of the lth path at the user side and $\psi_{U,l} \triangleq \frac{d_U \sin \vartheta_{U,l}}{\lambda_c}$ as the normalized AoD. Considering the delay differences among antennas at the user side and using the similar mathematical manipulations as in (1)-(6), the uplink frequency channel between the user and the BS can be arranged by a matrix as

$$\mathbf{H}(f) = \sum_{l=1}^{L} \alpha_l \mathbf{a}(\Xi_l(f)) \mathbf{a}_U^H(\Xi_{U,l}(f)) e^{-j2\pi f \tau_l}, \quad (7)$$

where

$$\mathbf{a}_U(\psi) \triangleq [1, e^{-j2\pi\psi}, \ldots, e^{-j2\pi(M_U-1)\psi}]^T \in \mathbb{C}^{M_U \times 1} \quad (8)$$

and

$$\Xi_{U,l}(f) \triangleq (1 + \frac{f}{f_c})\psi_{U,l}. \quad (9)$$

The (m, m')th element of $\mathbf{H}(f)$ in (7) denotes the frequency response between the mth antenna of the BS and the m'th antenna of the served user.

In a hybrid MIMO-OFDM system, denote the number of subcarriers as N and the subcarrier spacing as $\eta = W/N$. In terms of (7), the uplink channel at the nth subcarrier can be obtained as

$$\mathbf{H}_n = \sum_{l=1}^{L} \alpha_l \mathbf{a}(\Xi_l((n-1)\eta)) \mathbf{a}_U^H(\Xi_{U,l}((n-1)\eta)) e^{-j2\pi(n-1)\eta\tau_l}. \quad (10)$$

Denote the number of RF chains at the BS as N_{RF} and the number of input data streams as N_S, which satisfies $N_S \leq N_{\text{RF}} \leq M_U \leq M$. The downlink transmission process at the nth subcarrier can be expressed as

$$\mathbf{y}_n = \mathbf{H}_n^H \mathbf{F}_{\text{RF}} \mathbf{F}_{\text{BB},n} \mathbf{s}_n + \mathbf{n}_n, \quad (11)$$

where $\mathbf{F}_{\text{RF}} \in \mathbb{C}^{M \times N_{\text{RF}}}$ is the analog precoding matrix, $\mathbf{F}_{\text{BB},n} \in \mathbb{C}^{N_{\text{RF}} \times N_S}$ is the baseband digital precoding matrix, $\mathbf{s}_n$ is the transmitted data stream, and $\mathbf{n}_n$ is the additive noise at the nth subcarrier of the user.

III. Beam Squint on Hybrid Phased Array

The hybrid analog/digital architecture is commonly used to tackle large power consumption and high hardware cost. It largely reduces the number of RF chains and transfers part of signal processing task from digital baseband signal processor to analog beamformer/combiner. Since the hybrid beamforming with analog phase-shifting maximizes the hardware reuse in millimeter-wave communications [8], it becomes the most popular hybrid scheme among different implementations of analog beamformer/combiner. This result can also be applied

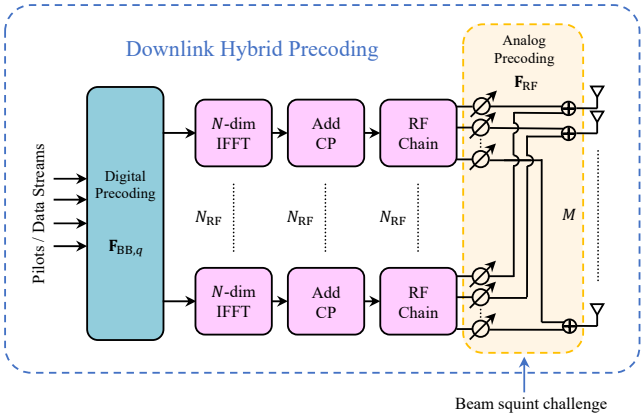

Fig. 2. The downlink hybrid precoding diagram based on phased array.

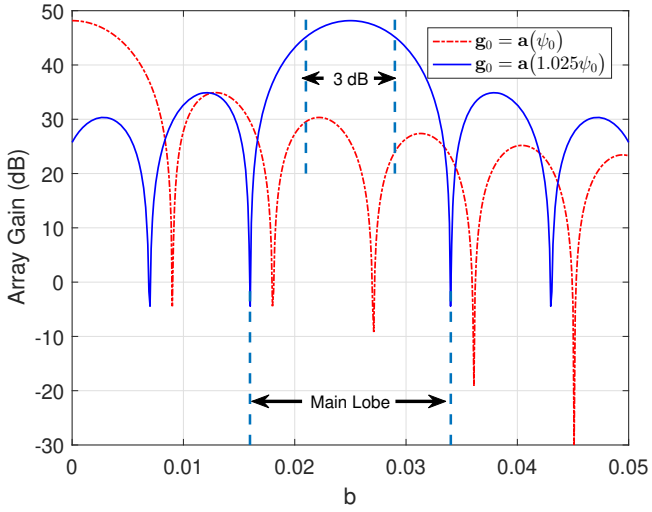

Fig. 3. The varying array gain over different frequencies due to beam squint.

in THz communications. In this paper, we investigates the phased array-based fully-connected hybrid beamforming architecture for THz communications, as shown in Fig. 2.

However, the hybrid architecture introduces additional constraints while simplifying the hardware implementation. For example, the number of simultaneously transmitted data streams is limited to the reduced number of RF chains and the beamforming ability is greatly restricted since the analog beamformer is only able to adjust the phase of RF signals and is not able to change the signal amplitude, etc. These constraints affect the system capacity compared with the full-digital architecture.

A remarkable challenge on hybrid phased array architecture in THz communications is beam squint. On one hand, a phase shifter is essentially the narrowband device as it can only generate the same phase shift at different frequencies. On the other hand, in order to maximize the array gain over the whole bandwidth, mitigating beam squint requires that each phase shifter should generate different phase shifts at different frequencies to form frequency-dependent steering vectors. This natural contradiction makes the optimal array gain only achievable at a given frequency. Specifically, for the incident path with AoA ϑ_0 and the corresponding normalized AoA $\psi_0 = \frac{d\sin\vartheta_0}{\lambda_c}$, if we design the phases for carrier frequency f_c and denote the phases at different phase shifters as $\mathbf{g}_0 \in \mathbb{C}^{M\times 1}$, $\mathbf{g}_0$ will be the fixed $\mathbf{a}(\psi_0)$. In this case, for baseband frequency f, the array gain should be

$$\begin{aligned}|\mathbf{a}^H(\Xi_l(f))\mathbf{g}_0| &= \left|\sum_{m=1}^{M} e^{j2\pi(m-1)\psi_0\frac{f}{f_c}}\right| \\ &= \left|\frac{\sin\left(\pi M\psi_0\frac{f}{f_c}\right)}{\sin\left(\pi\psi_0\frac{f}{f_c}\right)}\cdot e^{j\pi(M-1)\psi_0\frac{f}{f_c}}\right| \\ &= \left|\frac{\sin\left(\pi M\psi_0\frac{f}{f_c}\right)}{\sin\left(\pi\psi_0\frac{f}{f_c}\right)}\right|. \end{aligned} \tag{12}$$

Clearly, when $f \neq f_c$, the array gain is smaller than $|\mathbf{a}^H(\psi_0)\mathbf{g}_0| = M$ and would be zero when $\frac{f}{f_c} = \frac{k}{M\psi_0}$, $k = 1, 2, \ldots, \lfloor M\psi_0 \rfloor$.

Denote $b \triangleq \frac{f}{f_c}$. Fig. 3 illustrates an example in the dotted curve of the array gain over different frequencies when $\mathbf{g}_0 = \mathbf{a}(\psi_0)$, $M = 256$, $\vartheta_0 = \frac{\pi}{3}$, $\psi_0 = \frac{d\sin\vartheta_0}{\lambda_c}$, and $d = \frac{1}{2}\lambda_c$. It also illustrates in the solid curve the case when the phases are designed for frequency $f_c + \frac{W}{2}$ and $W = 0.05f_c$, i.e., $\mathbf{g}_0 = \mathbf{a}\big((1+\frac{W}{2f_c})\psi_0\big) = \mathbf{a}\big(1.025\psi_0\big)$. If we ignore the beam squint, $\mathbf{g}_0$ for both cases would be the optimal phases for the path with normalized angle ψ_0; $\mathbf{a}(\psi_0)$ as well as $\mathbf{a}\big(1.025\psi_0\big)$ would give the almost equal array gain over the whole frequency band. However, with beam squint, the array gain over different frequencies varies tremendously. It is easy to conclude that

- when $b > \frac{0.886}{M\psi_0}$, it is inevitable that some frequencies will fall out of 3 dB bandwidth [1], i.e., the array gains at these frequencies will be less than $\sqrt{\frac{M}{2}}$;
- when $b > \frac{2}{M\psi_0}$, some frequencies will fall out of the main lobe, i.e., the array gains at these frequencies become significantly attenuate and could even be zero.

Based on the above discussion, the irreconcilable contradiction caused by the beam squint effect basically lies in the analog part in a transceiver, specifically the section between the antennas and the RF chain, as shown in the shadow of Fig. 2. Therefore, the redesign of analog precoding algorithm and/or the redesign of the analog precoding hardware implementation are critical to mitigating the beam squint issue. In the following two sections, we will propose two approaches to beam squint alleviation. Section IV inherits the fully-connected phase shifter-based analog beamformer but develops a new analog beamforming technique which can generate wider beams to make the array gains at different frequencies evenly distributed. Section V introduces a few true-time-delay (TTD) lines to compensate the non-negligible differences of time delays among different antennas, rebuild the transmission

[1]The 3 dB bandwidth here is known as the half-power bandwidth in frequency domain, at which point the output power has dropped to half of its peak value, and thus this point in the logarithmic scale is 3 dB. In antennas and array signal processing, there is another concept called the beam width adopted in the next section, which is also defined by the 3 dB points in angle domain. The power outside the pair of 3 dB points in angle domain is less than half at the antenna boresight.

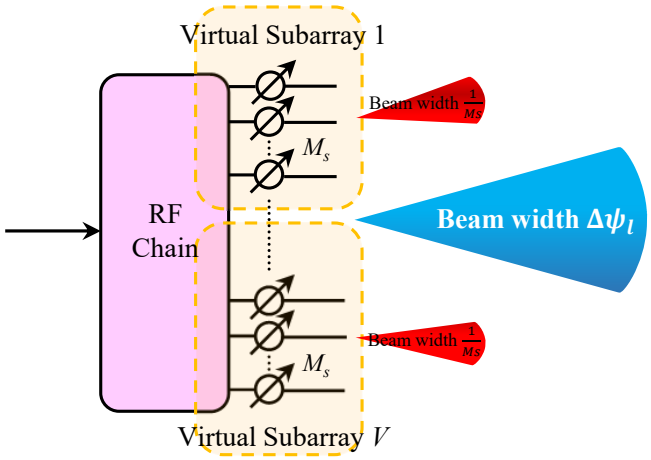

Fig. 4. Diagram of the proposed analog beam broadening design.

model, and redesigns the hardware implementation of the analog part in a transceiver to achieve the performance close to the full-digital architecture.

IV. Hybrid Beamforming Design with Beam Broadening

If we keep the current hardware implementation, one possible solution to alleviate the array gain discrepancy caused by beam squint, as shown in Fig. 3, is redesigning the analog beamforming algorithm in order to broaden the beam such that the array gain can be even over the operating frequency range. In this section, we propose a beam broaden approach by dividing the phase shifters connected to each RF chain into several groups. Each group has the same number of phase shifters and generates a narrow sub-beam, so that a wider beam can be obtained by combining different sub-beams together, as shown in Fig. 4. Denote the number of phase shifters in each group as M_s. The number of groups will be $V = \lfloor \frac{M}{M_s} \rfloor$.

A. Analog Beam Broadening with Virtual Sub-Arrays

According to the array signal processing theory [37], the beam width produced by the steering vector in (5) is $\frac{1}{M_s}$ in the normalized angle domain[2] for a ULA with M_s antennas. In the proposed design, one RF chain and its associated phase shifters are designed to cope with one channel path thanks to the linearity of channel paths. Basically, for the path with normalized angle ψ_l, since a beam with normalized angle ψ_l could be maximally squinted by $\Delta\psi_l = \Xi_l(W) - \Xi_l(0) = \frac{W}{f_c}\psi_l$ over the whole bandwidth, we propose to generate a beam with the total beam width $\Delta\psi_l$ so that the user can be covered by all frequency components of the transmitted signal even with beam squint. Therefore, the number of groups should satisfy

$$\frac{1}{M_s} \cdot V = \frac{1}{M_s} \cdot \lfloor \frac{M}{M_s} \rfloor \geq \Delta\psi_l. \tag{13}$$

[2]In this paper, all the beam width are defined in the normalized angle domain unless otherwise mentioned.

From (13), the maximum possible value of M_s satisfies $\frac{1}{M_s} \cdot \frac{M}{M_s} \geq \Delta\psi_l$ such that

$$M_s \leq \sqrt{\frac{M}{\Delta\psi_l}} \tag{14}$$

and the minimum possible value of M_s satisfies $\frac{1}{M_s} \cdot (\frac{M}{M_s} - 1) \geq \Delta\psi_l$ such that

$$M_s \geq \frac{\sqrt{1 + 4M\Delta\psi_l} - 1}{2\Delta\psi_l}. \tag{15}$$

It could be easily verified that

$$\frac{\sqrt{1 + 4M\Delta\psi_l} - 1}{2\Delta\psi_l} \leq \sqrt{\frac{M}{\Delta\psi_l}}. \tag{16}$$

Combining (14) and (15), the solution to M_s could be chosen from a small set of integers as

$$M_s = \max\left\{ M_s \in \mathbb{N} \,\middle|\, \frac{\sqrt{1 + 4M\Delta\psi_l} - 1}{2\Delta\psi_l} \leq M_s \leq \sqrt{\frac{M}{\Delta\psi_l}} \right. \\ \left. \text{and} \quad \frac{1}{M_s} \cdot \lfloor \frac{M}{M_s} \rfloor \geq \Delta\psi_l \right\}. \tag{17}$$

The antennas corresponding to each group can be regarded as a virtual sub-array. Selecting the following beamforming vector

$$\mathbf{a}_s(\tilde{\psi}_{l,v}) = [1, e^{-j2\pi\tilde{\psi}_{l,v}}, \ldots, e^{-j2\pi(M_s-1)\tilde{\psi}_{l,v}}]^T \in \mathbb{C}^{M_s \times 1} \tag{18}$$

for group $v \in \{1, \ldots, V\}$ ensures that the received signal at any frequency in the operating frequency band can be covered by the mainlobe of one virtual sub-array within its 3 dB beam width, where

$$\tilde{\psi}_{l,v} = \psi_l + \frac{1}{2M_s} + \frac{1}{M_s}(v-1) = \psi_l + \frac{2v-1}{2M_s}. \tag{19}$$

Accordingly, denote the phase shifts for the entire array as $\mathbf{g}_l \in \mathbb{C}^{M \times 1}$, which can be designed as

$$[\mathbf{g}_l]_{(v-1)M_s+m} = \begin{cases} \frac{1}{\sqrt{VM_s}} e^{-j2\pi[(v-1)M_s+(m-1)]\tilde{\psi}_{l,v}} e^{-j\phi_{l,v}}, \\ \qquad\qquad v \in [1, V] \text{ and } m \in [1, M_s] \\ 0, \qquad\qquad v > V \text{ or } m > M_s \end{cases} \tag{20}$$

Here, $e^{-j\phi_{l,v}}$ is introduced to smooth the phase change between adjacent sub-arrays without altering the steering vector of each sub-array to reduce the array gain variation in the normalized angle domain.

Since the middle of two beams in the normalized angle domain mostly tends to fluctuate, we propose to maximize the

array gain at the normalized angle $\frac{\tilde{\psi}_{l,v}+\tilde{\psi}_{l,v+1}}{2}$, the array gain of which can be calculated as

$$\begin{aligned}
&\left|\mathbf{a}^H\left(\frac{\tilde{\psi}_{l,v}+\tilde{\psi}_{l,v+1}}{2}\right)\mathbf{g}_l\right| = \left|\mathbf{a}^H\left(\psi_l+\frac{v}{M_s}\right)\mathbf{g}_l\right| \\
=&\left|\sum_{v'=1}^{V}\sum_{m=1}^{M_s}\frac{1}{\sqrt{VM_s}}e^{-j2\pi[(v'-1)M_s+(m-1)]\tilde{\psi}_{l,v'}}e^{-j\phi_{l,v'}}\right. \\
&\qquad\left.\times e^{j2\pi[(v'-1)M_s+(m-1)](\psi_l+\frac{v}{M_s})}\right| \\
=&\left|\frac{1}{\sqrt{VM_s}}\sum_{v'=1}^{V}\sum_{m=1}^{M_s}e^{-j2\pi[(v'-1)M_s+(m-1)](\psi_l+\frac{2v'-1}{2M_s})}e^{-j\phi_{l,v'}}\right. \\
&\qquad\left.\times e^{j2\pi[(v'-1)M_s+(m-1)](\psi_l+\frac{v}{M_s})}\right| \\
=&\left|\frac{1}{\sqrt{VM_s}}\sum_{v'=1}^{V}\sum_{m=1}^{M_s}e^{-j2\pi[(v'-1)M_s+(m-1)]\frac{2v'-2v-1}{2M_s}}e^{-j\phi_{l,v'}}\right| \\
=&\left|\frac{1}{\sqrt{VM_s}}\sum_{v'=1}^{V}e^{-j\pi(v'-1)(2v'-2v-1)}e^{-j\phi_{l,v'}}\right. \\
&\qquad\left.\times\sum_{m=1}^{M_s}e^{-j\pi\frac{m-1}{M_s}(2v'-2v-1)}\right|. \quad (21)
\end{aligned}$$

As $M_s \gg 1$ in general,

$$\left|\sum_{m=1}^{M_s}e^{-j\pi\frac{m-1}{M_s}(2v'-2v-1)}\right| = \frac{\sin(\pi(2v'-2v-1)/2)}{\sin(\pi(2v'-2v-1)/(2M_s))} \quad (22)$$

is a Dirichlet kernel, whose value is close to zero when $|(2v'-2v-1)/2| \geq 1$, i.e., we only need to count $v'=v$ and $v'=v+1$ in the summation of (22). In this way, (21) can be approximated as

$$\begin{aligned}
&\left|\mathbf{a}^H\left(\frac{\tilde{\psi}_{l,v}+\tilde{\psi}_{l,v+1}}{2}\right)\mathbf{g}_l\right| \\
\approx&\frac{1}{\sqrt{VM_s}}\left|e^{j\pi(v-1)}e^{-j\phi_{l,v}}\sum_{m=1}^{M_s}e^{j\pi\frac{m-1}{M_s}}\right. \\
&\qquad\left.+e^{-j\pi v}e^{-j\phi_{l,v+1}}\sum_{m=1}^{M_s}e^{-j\pi\frac{m-1}{M_s}}\right| \\
=&\frac{1}{\sqrt{VM_s}}\left|-e^{-j\phi_{l,v}}\sum_{m=1}^{M_s}e^{j\pi\frac{m-1}{M_s}}+e^{-j\phi_{l,v+1}}\sum_{m=1}^{M_s}e^{-j\pi\frac{m-1}{M_s}}\right| \\
=&\frac{1}{\sqrt{VM_s}\cdot\sin(\frac{\pi}{2M_s})}\left|-e^{-j\phi_{l,v}}e^{j\pi\frac{M_s-1}{2M_s}}+e^{-j\phi_{l,v+1}}e^{-j\pi\frac{M_s-1}{2M_s}}\right| \\
=&\frac{1}{\sqrt{VM_s}\cdot\sin(\frac{\pi}{2M_s})}\left|e^{j\pi\frac{M_s-1}{2M_s}}-e^{-j(\phi_{l,v+1}-\phi_{l,v})}e^{-j\pi\frac{M_s-1}{2M_s}}\right|. \quad (23)
\end{aligned}$$

Clearly, (23) can reach its maximum value when $e^{j\pi\frac{M_s-1}{2M_s}}$ and $-e^{-j(\phi_{l,v+1}-\phi_{l,v})}e^{-j\pi\frac{M_s-1}{2M_s}}$ have the same phase. Therefore, we should choose $\phi_{l,v}$ satisfying

$$\begin{aligned}
&\pi\cdot\frac{M_s-1}{2M_s} = \pi-(\phi_{l,v+1}-\phi_{l,v})-\pi\cdot\frac{M_s-1}{2M_s} \\
\Leftrightarrow\quad&\phi_{l,v+1}-\phi_{l,v} = \frac{\pi}{M_s}. \quad (24)
\end{aligned}$$

A possible solution to (24) is

$$\phi_{l,v} = (v-1)\frac{\pi}{M_s}, \quad v=1,\ldots,V. \quad (25)$$

By this means, the array gain at the normalized angle $\frac{\tilde{\psi}_{l,v}+\tilde{\psi}_{l,v+1}}{2}$ can be approximated as

$$\frac{1}{\sqrt{VM_s}\cdot\sin(\frac{\pi}{2M_s})}\times 2 \approx \frac{4}{\pi}\sqrt{\frac{M_s}{V}}. \quad (26)$$

The array gain at the steering angle corresponding to each virtual sub-array can be calculated as

$$\begin{aligned}
&\left|\mathbf{a}^H(\tilde{\psi}_{l,v})\mathbf{g}_l\right| = \left|\mathbf{a}^H\left(\psi_l+\frac{2v-1}{2M_s}\right)\mathbf{g}_l\right| \\
=&\left|\sum_{v'=1}^{V}\sum_{m=1}^{M_s}\frac{1}{\sqrt{VM_s}}e^{-j2\pi[(v'-1)M_s+(m-1)]\tilde{\psi}_{l,v'}}e^{-j\phi_{l,v'}}\right. \\
&\qquad\left.\times e^{j2\pi[(v'-1)M_s+(m-1)](\psi_l+\frac{2v-1}{2M_s})}\right| \\
=&\left|\frac{1}{\sqrt{VM_s}}\sum_{v'=1}^{V}\sum_{m=1}^{M_s}e^{-j2\pi[(v'-1)M_s+(m-1)](\frac{v'-v}{M_s})}e^{-j\pi\frac{v'-1}{M_s}}\right| \\
=&\left|\frac{1}{\sqrt{VM_s}}\sum_{v'=1}^{V}e^{-j2\pi(v'-1)(v'-v)}e^{-j\pi\frac{v'-1}{M_s}}\right. \\
&\qquad\left.\times\sum_{m=1}^{M_s}e^{-j2\pi\frac{m-1}{M_s}(v'-v)}\right|. \quad (27)
\end{aligned}$$

Similarly, we only need to count $v'=v$ in the summation of (27) when $M_s \gg 1$. As a result, $\left|\sum_{m=1}^{M_s}e^{-j2\pi\frac{m-1}{M_s}(v'-v)}\right| = \frac{\sin(\pi(v'-v))}{\sin(\pi(v'-v)/M_s)} \approx 0$ when $|v'-v| \geq 1$ and (27) can be approximated as

$$\left|\mathbf{a}^H(\tilde{\psi}_{l,v})\mathbf{g}_l\right| \approx \left|\frac{1}{\sqrt{VM_s}}e^{-j\pi\frac{v-1}{M_s}}\times M_s\right| = \sqrt{\frac{M_s}{V}}, \quad (28)$$

which demonstrates that the introduced $e^{-j\phi_{l,v}}$ can effectively enhance the array gain at $\frac{\tilde{\psi}_{l,v}+\tilde{\psi}_{l,v+1}}{2}$ and has no impact on the array gain at $\tilde{\psi}_{l,v}$.

Remark 1: The proposed virtual sub-array based beamforming design does not alter the hardware implementation of the conventional fully-connected hybrid architecture. The virtual sub-array is a concept that is conducive to understanding the mechanism of the analog beamformer design. Therefore, M_s can be regarded as an intermediate variable and the final output of this design is the value of $\mathbf{F}_{\text{RF}}$.

B. Array Gain over Different Frequencies

To determine the practical array gain at any given frequency $f \in [0, W]$, we rewrite f as

$$f = \frac{f_c}{M_s\psi_l}v_f + \frac{f_c}{M_s\psi_l}x - \frac{f_c}{2M_s\psi_l}, \quad (29)$$

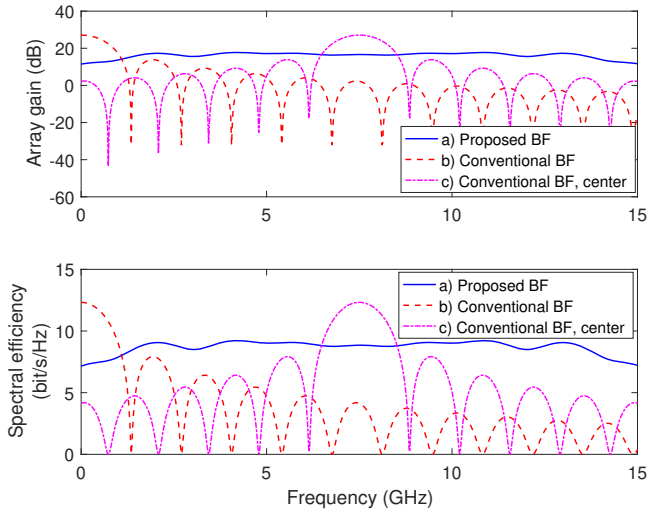

Fig. 5. Array gain across the whole frequency band of the proposed analog beamforming design with beam broadening.

where $v_f \in \{1, \ldots, V\}$ and $x \in [-\frac{1}{2}, \frac{1}{2})$. By this means, when $x \in [-\frac{1}{2}, 0) \bigcup (0, \frac{1}{2})$, the array gain, $|\mathbf{a}^H(\Xi_l(f))\mathbf{g}_l|$, can be approximately determined in Appendix A as

$$\sqrt{\frac{M_s}{V}}\sin(\pi|x|)\sqrt{\frac{1}{\pi^2x^2} - \frac{2\cos(2\pi x)}{\pi^2|x|(1-|x|)} + \frac{1}{\pi^2(1-|x|)^2}}. \tag{30}$$

When $x = 0$ and $x = -\frac{1}{2}$, the array gains are $\sqrt{\frac{M_s}{V}}$ and $\frac{4}{\pi}\sqrt{\frac{M_s}{V}}$, respectively, according to (26) and (28).

C. Average Array Gain and Performance Analysis

In Section IV-B, we obtain the array gain of the proposed analog beamforming design at any frequency $f \in [0, W]$. In this subsection, we derive the average array gain and analyze the performance of the proposed analog beamforming design.

It can be noted that

$$\begin{aligned}&\int_0^{\frac{1}{2}} \sqrt{\frac{1}{\pi^2x^2} - \frac{2\cos(2\pi x)}{\pi^2x(1-x)} + \frac{1}{\pi^2(1-x)^2}}\ dx \\ &= \int_{-\frac{1}{2}}^{0} \sqrt{\frac{1}{\pi^2x^2} + \frac{2\cos(2\pi x)}{\pi^2x(x+1)} + \frac{1}{\pi^2(x+1)^2}}\ dx.\end{aligned} \tag{31}$$

After dividing f as (29), the average array gain over $[0, W]$ can be calculated as

$$\begin{aligned}\mathbb{E}\{|\mathbf{a}^H(\Xi_l(f))\mathbf{g}_l|\} = \frac{1}{W}\Bigg[&2(V-1)E_S \cdot \frac{f_c}{M_s\psi_l} \\ &+ \int_{(V-1)\frac{f_c}{M_s\psi_l}}^{W} |\mathbf{a}^H(\Xi_l(f))\mathbf{g}_l| df\Bigg],\end{aligned} \tag{32}$$

where

$$E_S = \int_0^{\frac{1}{2}} \sqrt{\frac{M_s}{V}}\sin(\pi x)\sqrt{\frac{1}{\pi^2x^2} - \frac{2\cos(2\pi x)}{\pi^2x(1-x)} + \frac{1}{\pi^2(1-x)^2}}dx. \tag{33}$$

Since E_S is a definite integral, the value of E_S can be numerically integrated as

$$E_S \approx 0.5152\sqrt{\frac{M_s}{V}}. \tag{34}$$

Due to the inexistence of the closed-form expression of $\int_{(V-1)\frac{f_c}{M_s\psi_l}}^{W} |\mathbf{a}^H(\Xi_l(f))\mathbf{g}_l| df$, we can fit it by a polynomial as in (35) on the top of the next page, where $x_W \triangleq \frac{M_s\psi_l W}{f_c} - V + \frac{1}{2}$. As a result, the average array gain in (32) can be determined by (34) and (35) as in (36) on the top of the next page.

The array gain in (36) is an intuitive result since $\mathbb{E}\{|\mathbf{a}^H(\Xi_l(f))\mathbf{g}_l|\} \to 2E_S \approx 1.0304\sqrt{M_s/V}$ as V becomes large. The proposed analog beamforming design sacrifices part of array gain to make the power evenly distributed across the whole operating frequency band.

Fig. 5 illustrates an example of the array gain variation of the proposed analog beamforming design over different frequencies, where the path angle is $\vartheta_l = 60°$, the antenna spacing is $d = \frac{1}{2}\lambda_c$, $\psi_l = \frac{\sqrt{3}}{4}$, and the other system parameters are $M = 512$, $W = 15$ GHz, $f_c = 300$ GHz. For comparison, the conventional beamforming approaches with steering vectors $\mathbf{a}(\psi_l)$ (corresponding to curve b in Fig. 5) and $\mathbf{a}(1.025\psi_l)$ (corresponding to curve c in Fig. 5) respectively, are also plotted. In this example, the average array gains across the whole frequency band of curves a, b, and c in Fig. 5 is 6.5206, 2.1986, and 3.8107, respectively. Under the above system parameters, we also show the spectral efficiency between a single-antenna user and the BS for a LoS channel with $\vartheta_l = 60°$ and SNR = 10 dB, which intuitively reflects the improvement of the proposed virtual array-based analog beamforming approach in terms of capacity. The average spectral efficiencies across the whole frequency band of curves a, b, and c in Fig. 5 are 8.6921, 3.6448, and 5.3197, respectively.

D. Hybrid Precoding Design with Beam Broadening

Based on the results in Section IV-A and according to $\mathbf{g}_l$ in (20), we can design the analog beamformer with beam broadening for each path and obtain $\mathbf{F}_{\text{RF}}$. In a MIMO-OFDM system, the downlink transmission process can be written as (11) such that the optimal digital precoder with given $\mathbf{F}_{\text{RF}}$ is equivalent to maximizing the mutual information as

$$\begin{aligned}\mathbf{F}_{\text{BB},n}^{\text{opt}} = \arg\max \Bigg\{ &\frac{1}{N}\sum_{n=1}^{N} \log_2\left(\left|\mathbf{I}_{M_U}\right.\right. \\ &\left.\left. + \frac{\rho}{N_S}\mathbf{H}_n^H\mathbf{F}_{\text{RF}}\mathbf{F}_{\text{BB},n}\mathbf{F}_{\text{BB},n}^H\mathbf{F}_{\text{RF}}^H\mathbf{H}_n\right|\right)\Bigg\} \\ \text{s.t.} \quad &\sum_{n=1}^{N}\|\mathbf{F}_{\text{RF}}\mathbf{F}_{\text{BB},n}\|_F^2 = NN_S.\end{aligned} \tag{37}$$

Let $\mathbf{F}_{\text{BB},n} = \left(\mathbf{F}_{\text{RF}}^H\mathbf{F}_{\text{RF}}\right)^{-\frac{1}{2}}\tilde{\mathbf{F}}_{\text{BB},n}$ to decouple the power constraint in (37). The maximization problem in (37) is then converted to the singular value decomposition (SVD) problem. We summarize the hybrid precoding algorithm with

$$\int_{(V-1)\frac{f_c}{M_s\psi_l}}^{W}|\mathbf{a}^H(\Xi_l(f))\mathbf{g}_l|df \approx \begin{cases}\frac{f_c}{M_s\psi_l}E_S+\frac{f_c}{M_s\psi_l}\sqrt{\frac{M_s}{V}}(1.2373x_W^3-0.4391x_W^2+0.9441x_W), & 0<x_W\le\frac{1}{2}\\ \frac{f_c}{M_s\psi_l}\sqrt{\frac{M_s}{V}}(1.2373x_W^3+0.4391x_W^2+0.9441x_W+0.5152), & \frac{1}{2}<x_W\le 0\end{cases} \tag{35}$$

$$\begin{aligned}&\mathbb{E}\{|\mathbf{a}^H(\Xi_l(f))\mathbf{g}_l|\}\\ &\approx\begin{cases}\frac{2}{2V-1+2x_W}\left[(2V-1)E_S+\sqrt{\frac{M_s}{V}}(1.2373x_W^3-0.4391x_W^2+0.9441x_W)\right], & 0<x_W\le\frac{1}{2}\\ \frac{2}{2V-1+2x_W}\left[(2V-2)E_S+\sqrt{\frac{M_s}{V}}(1.2373x_W^3+0.4391x_W^2+0.9441x_W+0.5152)\right], & -\frac{1}{2}<x_W\le 0\end{cases}\end{aligned} \tag{36}$$

the proposed analog beam broadening method in this section as follows:

- **Step 1: Input** $\mathbf{H}_n$ in (10) and the corresponding channel parameters ψ_l, τ_l and α_l.
- **Step 2:** Arrange the channel parameters subject to $\alpha_1 \ge \alpha_2 \ge \cdots \ge \alpha_L$.
- **Step 3:** For each $l \in \{1,\ldots,N_{\text{RF}}\}$[3], determine $\Delta\psi_l = \frac{W}{f_c}\psi_l$ and the corresponding M_s in terms of (17); determine $\mathbf{g}_l$ in (20) with $\tilde{\psi}_{l,v}$ in (19) and $\phi_{l,v}$ in (25).
- **Step 4:** Build $\mathbf{F}_{\text{RF}} = [\mathbf{g}_1,\ldots,\mathbf{g}_{N_{\text{RF}}}]$.
- **Step 5:** Calculate $\tilde{\mathbf{H}}_n = \mathbf{H}_n^H\mathbf{F}_{\text{RF}}\left(\mathbf{F}_{\text{RF}}^H\mathbf{F}_{\text{RF}}\right)^{-\frac{1}{2}}$ and obtain its SVD as $\tilde{\mathbf{H}}_n = \tilde{\mathbf{U}}_n\tilde{\mathbf{\Sigma}}_n\tilde{\mathbf{V}}_n^H$.
- **Step 6:** Determine $\mathbf{F}_{\text{BB},n} = \left(\mathbf{F}_{\text{RF}}^H\mathbf{F}_{\text{RF}}\right)^{-\frac{1}{2}}[\tilde{\mathbf{V}}_n]_{:,1:N_S}$.
- **Step 7: Output** $\mathbf{F}_{\text{RF}}$ in Step 4 and $\mathbf{F}_{\text{BB},n}$ in Step 6.

Remark 2: In this paper, we assume that the channel and the path angles are known for precoding design. These channel information can actually be obtained by various angle-based channel estimation approaches, such as [24], [25], at the channel estimation stage.

V. Enhanced Hybrid Beamforming with True-Time-Delay Lines

In the last section, we divide the whole antenna array into several virtual sub-arrays and design an analog beamforming approach with the help of beam broadening. This approach renders the array gain evenly distributed across the whole operating frequency band as much as possible to mitigate the impact of beam squint. However, as shown in the example of Fig. 5, although the beam broadening based approach can achieve the much larger average array gain and higher average spectral efficiency compared with the conventional narrowband beamforming techniques that ignores beam squint, the roughly estimated array gain of the proposed beam broadening based approach is only $1.0304\sqrt{M_s/V}$, much lower than $\sqrt{M}$, the maximum array gain of the conventional beamforming technique at a certain frequency. Actually, the beam broadening based approach does not address the contradiction, which is discussed in Section III and caused by beam squint in analog hardware implementation of phased arrays-based hybrid transceivers, thus can only partially mitigate the impact of beam squint.

Since beam squint essentially results from the propagation delay across the antenna array aperture, a reasonable way to mitigate it is to compensate such propagation delay in time domain. In this section, we introduce TTD lines to enable wideband beamforming of the analog part in hybrid transceivers by compensating the propagation delay across the array aperture to thoroughly eliminate this contradiction.

A. True-Time-Delay Lines Based Analog Beamforming Design

According to the discussion in Section III, we need to redesign the part between the antennas and the RF chain, as shown in the shadow of Fig. 2. Since TTD lines are more expensive compared to phase shifters, we only adopt a few TTD lines, instead of replacing all phase shifters with TTD lines, and deploy the TTD lines between each RF chain and the phase shifters connected to each RF chain, as shown in Fig. 6. Specifically, M phase shifters connected to the same RF chain are divided into V_{TTD} groups, each corresponding to a TTD line. As a result, each group has $M_T = \frac{M}{V_{TTD}}$ phase shifters.

Due to the linearity of the multipath components and the linearity of the signals at the BS antennas from multiple RF chains, we consider a one-path channel and the transmission model between one RF chain at the BS and the user in this subsection for analysis simplicity. With the help of TTD lines, the combination of the mth phase shifter and the corresponding vth TTD line can be viewed as a wideband device, whose time-domain response can be expressed as

$$\frac{1}{\sqrt{M}}\cdot e^{-j2\pi(m-1)\tilde{\psi}_l}\cdot\delta(t-t_{l,v}). \tag{38}$$

Here, $\tilde{\psi}_l$ is the steering angle for the lth path and $t_{l,v}$ is the time delay provided by the vth TTD lines of this RF chain, where $v = \lceil\frac{m}{M_T}\rceil$. The corresponding frequency response of (38) can then be expressed as

$$g_{l,m}(f) = \frac{1}{\sqrt{M}}e^{-j2\pi(m-1)\tilde{\psi}_l}e^{-j2\pi f t_{l,v}}. \tag{39}$$

[3]When $L > N_{\text{RF}}$, one or several paths with smallest complex gains will be ignored. When $L < N_{\text{RF}}$, we can simply assume that $\alpha_{L+1} = \cdots = \alpha_{N_{\text{RF}}} = 0$.

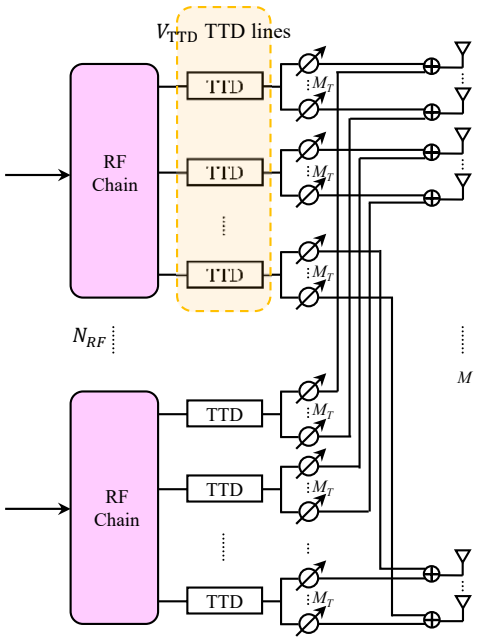

Fig. 6. Diagram of the proposed analog beamforming design with true-time-delay lines.

Denote $\mathbf{g}_l(f) \triangleq [g_1(f), \ldots, g_M(f)]^T$. For baseband frequency f, the array gain should be

$$\begin{aligned}
&|\mathbf{a}^H(\Xi_l(f))\mathbf{g}_l(f)| \\
=&\frac{1}{\sqrt{M}}\left|\sum_{m=1}^{M} e^{-j2\pi(m-1)\tilde{\psi}_l} e^{-j2\pi f t_{l,v}} e^{j2\pi(m-1)\psi_l(1+\frac{f}{f_c})}\right| \\
=&\frac{1}{\sqrt{M}}\left|\sum_{m=1}^{M} e^{-j2\pi(m-1)(\tilde{\psi}_l-\psi_l)} e^{-j2\pi f t_{l,v}} e^{j2\pi(m-1)\psi_l\frac{f}{f_c}}\right|
\end{aligned} \tag{40}$$

Our goal is to choose $\tilde{\psi}_l$ and $t_{l,v}$ that maximize the array gain. To simplify analysis, denote $\tilde{t}_{l,v} \triangleq t_{l,v} - (v-1)M_T\frac{\psi_l}{f_c}$ and $\tilde{f} = f - \frac{W}{2}$. Substituting $\tilde{t}_{l,v}$ and $\tilde{f}$ back to (40) yields

$$\begin{aligned}
|\mathbf{a}^H(\Xi_l(f))\mathbf{g}_l(f)| =& \frac{1}{\sqrt{M}}\left|\sum_{m=1}^{M} e^{-j2\pi(m-1)(\tilde{\psi}_l-\psi_l-\psi_l\frac{W}{2f_c})}\right. \\
&\left.\times\, e^{-j2\pi(\tilde{f}+\frac{W}{2})(\tilde{t}_{l,v}+(v-1)M_T\frac{\psi_l}{f_c})} e^{j2\pi(m-1)\psi_l\frac{\tilde{f}}{f_c}}\right| \\
=&\frac{1}{\sqrt{M}}\left|\sum_{v=1}^{V_{TTD}}\sum_{m=1}^{M_T} e^{-j2\pi[(v-1)M_T+(m-1)](\tilde{\psi}_l-\psi_l-\psi_l\frac{W}{2f_c})}\right. \\
&\left.\times\, e^{-j2\pi(\tilde{f}+\frac{W}{2})(\tilde{t}_{l,v}+(v-1)M_T\frac{\psi_l}{f_c})} e^{j2\pi[(v-1)M_T+(m-1)]\psi_l\frac{\tilde{f}}{f_c}}\right| \\
=&\frac{1}{\sqrt{M}}\left|\sum_{v=1}^{V_{TTD}} e^{-j2\pi(v-1)M_T(\tilde{\psi}_l-\psi_l-\psi_l\frac{W}{2f_c})} e^{-j2\pi\tilde{f}\tilde{t}_{l,v}}\right. \\
&\left.\times\, \gamma_{l,v}\sum_{m=1}^{M_T} e^{-j2\pi(m-1)\left[\tilde{\psi}_l-\psi_l-\psi_l\frac{W}{2f_c}-\psi_l\frac{\tilde{f}}{f_c}\right]}\right| \\
=&\frac{1}{\sqrt{M}}\left|\sum_{v=1}^{V_{TTD}} \gamma_{l,v} e^{-j2\pi(v-1)M_T(\tilde{\psi}_l-\psi_l-\psi_l\frac{W}{2f_c})} e^{-j2\pi\tilde{f}\tilde{t}_{l,v}}\right| \\
&\times \frac{\sin(\pi M_T(\tilde{\psi}_l-\psi_l-\psi_l\frac{W}{2f_c}-\psi_l\frac{\tilde{f}}{f_c}))}{\sin(\pi(\tilde{\psi}_l-\psi_l-\psi_l\frac{W}{2f_c}-\psi_l\frac{\tilde{f}}{f_c}))},
\end{aligned} \tag{41}$$

where $\gamma_{l,v} = e^{-j2\pi\frac{W}{2}(\tilde{t}_{l,v}+(v-1)M_T\frac{\psi_l}{f_c})}$. Similar to Section IV, we introduce the additional phase shift, $e^{-j\phi_{l,v}}$, for each group to smooth the phase change between adjacent phase shifters belonging to different groups. Hence, the frequency response in (39) becomes

$$g_{l,m}(f) = \frac{1}{\sqrt{M}} e^{-j2\pi(m-1)\tilde{\psi}_l} e^{-j\phi_{l,v}} e^{-j2\pi f t_{l,v}} \tag{42}$$

and the array gain $|\mathbf{a}^H(\Xi_l(f))\mathbf{g}_l(f)|$ will be

$$\begin{aligned}
&\frac{1}{\sqrt{M}}\left|\sum_{v=1}^{V_{TTD}} \gamma_{l,v} e^{-j2\pi(v-1)M_T(\tilde{\psi}_l-\psi_l-\psi_l\frac{W}{2f_c})} e^{-j2\pi\tilde{f}\tilde{t}_{l,v}} e^{-j\phi_{l,v}}\right| \\
&\times \frac{\sin(\pi M_T(\tilde{\psi}_l-\psi_l-\psi_l\frac{W}{2f_c}-\psi_l\frac{\tilde{f}}{f_c}))}{\sin(\pi(\tilde{\psi}_l-\psi_l-\psi_l\frac{W}{2f_c}-\psi_l\frac{\tilde{f}}{f_c}))}.
\end{aligned} \tag{43}$$

In this case, one of the solutions to maximizing the array gain is

$$\begin{cases}
\tilde{\psi}_l = \psi_l + \psi_l\dfrac{W}{2f_c} \\
\tilde{t}_{l,v} = 0 \quad \Leftrightarrow \quad t_{l,v} = (v-1)M_T\dfrac{\psi_l}{f_c} \\
e^{-j\phi_{l,v}} = \gamma_{l,v}^* \quad \Leftrightarrow \quad \phi_{l,v} = -\pi(v-1)M_T\psi_l\dfrac{W}{f_c}
\end{cases} \tag{44}$$

and the maximum array gain is

$$\begin{aligned}
|\mathbf{a}^H(\Xi_l(f))\mathbf{g}_l(f)| &= \frac{V_{TTD}}{\sqrt{M}}\frac{\sin(\pi M_T\psi_l\frac{\tilde{f}}{f_c})}{\sin(\pi\psi_l\frac{\tilde{f}}{f_c})} \\
&= \sqrt{M}\cdot\frac{\sin(\pi M_T\frac{\psi_l}{f_c}(f-\frac{W}{2}))}{M_T\sin(\pi\frac{\psi_l}{f_c}(f-\frac{W}{2}))}.
\end{aligned} \tag{45}$$

According to (45), the array gain at $f = \frac{W}{2}$ is $\sqrt{M}$, which is maximum value over the whole frequency band. Besides, to ensure the whole frequency band lies within the mainlobe and the 3 dB bandwidth, the number of antennas in each group should satisfy $M_T < \frac{2f_c}{W\psi_l}$ and $M_T < \frac{f_c}{2W\psi_l}$, respectively.

B. Selection of M_T and Performance Analysis

Based on the result in Section V-A, to avoid the dramatic variation of the array gain across the whole frequency band shown in Fig. 3, a necessary condition is $M_T < \frac{f_c}{2W\psi_l}$ to ensure that the received signal at any frequency f lies inside the 3 dB bandwidth and has at least half power at the center frequency $f = \frac{W}{2}$. On the other hand, M_T should satisfy $M_T \gg 1$ since a relatively large M_T is required to reduce the hardware cost and power consumption. For an extreme case that $M_T = 1$, the array gain would be constant $\sqrt{M}$, which, however, would make all phase shifters meaningless

and dramatically increase hardware cost and implementation complexity. In this subsection, we derive the average array gain and the achievable rate for the LoS case of the proposed approach and investigate the selection of M_T for different requirements.

Denote $\mathrm{Si}(x) \triangleq \int_0^x \frac{\sin t}{t} dt$ as the sinc integral function. In terms of (45), the average array gain can be calculated as

$$\begin{aligned}
&\mathbb{E}\{|\mathbf{a}^H(\Xi_l(f))\mathbf{g}_l(f)|\} = \frac{\sqrt{M}}{W}\int_0^W \frac{\sin(\pi M_T \frac{\psi_l}{f_c}(f-\frac{W}{2}))}{M_T \sin(\pi \frac{\psi_l}{f_c}(f-\frac{W}{2}))} df \\
=&\frac{2\sqrt{M}}{W}\int_0^{\frac{W}{2}} \frac{\sin(\pi M_T \psi_l \frac{\tilde{f}}{f_c})}{M_T \sin(\pi \psi_l \frac{\tilde{f}}{f_c})} d\tilde{f} \\
\approx&\frac{2\sqrt{M}}{W}\int_0^{\frac{W}{2}} \frac{\sin(\pi M_T \psi_l \frac{\tilde{f}}{f_c})}{\pi M_T \psi_l \frac{\tilde{f}}{f_c}} d\tilde{f} \\
=&\frac{2\sqrt{M}}{W}\frac{f_c}{\pi M_T \psi_l}\mathrm{Si}\left(\pi M_T \frac{W\psi_l}{2f_c}\right) \\
\approx&\sqrt{M}\left(1-\frac{1}{72}M_T^2\pi^2\psi_l^2\frac{W^2}{f_c^2}\right),
\end{aligned} \tag{46}$$

where the first approximation holds when $M_T \gg 1$ and the second approximation uses the cubic polynomial to fit $\mathrm{Si}(x)$ since $\mathrm{Si}(x)$ has no closed-form expression. As a comparison, the array gain of the full-digital beamforming is $\sqrt{M}$. If we require that the proposed beamforming approach should achieve the average array gain of $\zeta\sqrt{M}$, $0 < \zeta < 1$, M_T needs to satisfy

$$M_T < \sqrt{\frac{72(1-\zeta)f_c^2}{\pi^2\psi_l^2 W^2}} \quad \Rightarrow \quad M_T = \left\lfloor \sqrt{\frac{72(1-\zeta)f_c^2}{\pi^2\psi_l^2 W^2}} \right\rfloor. \tag{47}$$

Based on (45), we can also obtain the achievable rate for a LoS channel between a single-antenna user and the BS. Denote ρ as the SNR at the user side. The downlink spectral efficiency can be calculated as

$$\begin{aligned}
R_E &= \frac{1}{W}\int_0^W \log_2\left(1+\rho\frac{\sin^2(\pi M_T\frac{\psi_l}{f_c}(f-\frac{W}{2}))}{M_T\sin^2(\pi\frac{\psi_l}{f_c}(f-\frac{W}{2}))}\right)df \\
&= \frac{2}{W}\int_0^{\frac{W}{2}} \log_2\left(1+\rho\frac{\sin^2(\pi M_T\frac{\psi_l}{f_c}f)}{M_T\sin^2(\pi\frac{\psi_l}{f_c}f)}\right)df \\
&\approx \frac{2}{W}\int_0^{\frac{W}{2}} \log_2\left(1+\rho\frac{\sin^2(\pi M_T\frac{\psi_l}{f_c}f)}{\pi^2 M_T^2\frac{\psi_l^2}{f_c^2}f^2}\right)df \\
&= \frac{2}{W}\frac{f_c}{\pi M_T\psi_l}\int_0^{\frac{\pi M_T\psi_l W}{2f_c}} \log_2\left(1+\rho\frac{\sin^2 x}{x^2}\right)dx,
\end{aligned} \tag{48}$$

where the approximation in (48) holds when $M_T \gg 1$. By using the quadratic polynomial $1-\frac{x^2}{3!}$ to approximate $\frac{\sin x}{x}$, (48) can be expressed as

$$\begin{aligned}
R_E &\approx \frac{2}{W}\frac{f_c}{\pi M_T\psi_l}\int_0^{\frac{\pi M_T\psi_l W}{2f_c}} \log_2\left(1+\rho\left(1-\frac{x^2}{3!}\right)^2\right)dx \\
&\approx \frac{2}{W}\frac{f_c}{\pi M_T\psi_l}\int_0^{\frac{\pi M_T\psi_l W}{2f_c}} \log_2\left(1+\rho-\frac{\rho}{3}x^2\right)dx
\end{aligned}$$

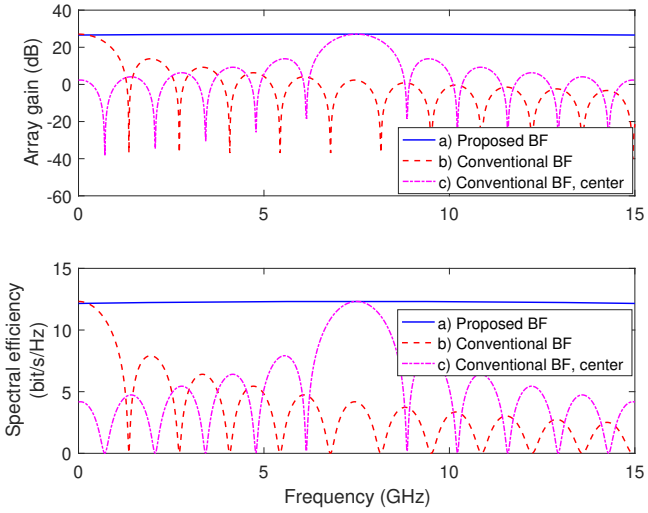

Fig. 7. Array gain across the whole frequency band of the proposed analog beamforming design based on TTD lines.

$$\begin{aligned}
&= \frac{2}{W}\frac{f_c}{\pi M_T\psi_l}\sqrt{\frac{3}{\rho}}\int_0^{\sqrt{\frac{\rho}{3}}\frac{\pi M_T\psi_l W}{2f_c}} \log_2(1+\rho-x^2)dx \\
&= \frac{2}{W}\frac{f_c}{\pi M_T\psi_l}\sqrt{\frac{3}{\rho}}\Bigg[x\log_2|1+\rho-x^2| - \frac{2}{\ln 2}x \\
&\qquad + \sqrt{1+\rho}\log_2\left|\frac{\sqrt{1+\rho}+x}{\sqrt{1+\rho}-x}\right|\Bigg]_0^{\sqrt{\frac{\rho}{3}}\frac{\pi M_T\psi_l W}{2f_c}} \\
&= \log_2\left|1+\rho-\frac{\rho}{12}\frac{\pi^2 M_T^2\psi_l^2 W^2}{f_c^2}\right| - \frac{2}{\ln 2} \\
&\quad + \sqrt{3+\frac{3}{\rho}}\log_2\frac{2f_c}{\pi M_T\psi_l W}\left|\frac{\sqrt{1+\rho}+\sqrt{\frac{\rho}{3}}\frac{\pi M_T\psi_l W}{2f_c}}{\sqrt{1+\rho}-\sqrt{\frac{\rho}{3}}\frac{\pi M_T\psi_l W}{2f_c}}\right|,
\end{aligned} \tag{49}$$

where the second approximation ignores the small quartic item.

Fig. 7 presents an example of the proposed TTD based analog beamforming design in a LoS channel with path angle $\vartheta_l = 60°$ and antenna spacing $d = \frac{1}{2}\lambda_c$. The system parameters are set as $M = 510$, $W = 15$ GHz, $f_c = 300$ GHz. Similar to Fig. 5, the conventional beamforming approaches with steering vectors $\mathbf{a}(\psi_l)$ and $\mathbf{a}(1.025\psi_l)$ are also provided in this figure for comparison. In this example, we expect the average array gain to be 98% of that in full-digital beamforming. Thus, we select $M_T = 17$ in terms of (47). The average array gains across the whole frequency band of curves a, b, and c in Fig. 7 is 22.1686, 2.2023, and 3.8130, respectively. Under the above system parameters, the average spectral efficiency between a single-antenna user and the BS in a LoS channel with $\vartheta_l = 60°$ and SNR = 10 dB of curves a, b, and c in Fig. 5 is 12.2627, 3.6538, and 5.3193, respectively. Note that the theoretical average array gain in (46) and average spectral efficiency in (49) are 22.1638 and 12.2611 bits/s/Hz, respectively, where the normalized deviations between the approximated theoretical values and the numerical results are less than 0.2% and 0.1%, respectively. Compared with the beam broadening approach in Section IV, the proposed approach in this section further

enhances the average array gain and spectral efficiency by enabling the wideband beamforming ability for analog part in hybrid transceivers with the help of TTD lines and achieves the performance close to the full-digital transceivers.

C. TTD-Based Hybrid Precoding Design

After introducing the TTD lines, the downlink transmission cannot be expressed as (11) since (11) does not consider the impact of the TTD lines. Denote $t_{l,v}$ as the time delay set for the vth TTD line connected to the lth RF chain. Since the time-domain delay corresponds to the phase shift in frequency domain, the delay $t_{l,v}$ produces $-2\pi f t_{l,v}$ of phase change at frequency f. Considering the effect of the TTD lines, the downlink transmission at the nth subcarrier in (11) should be modified as

$$\mathbf{y}_n = \mathbf{H}^H\big(\mathbf{F}_{\text{RF}} \odot \mathbf{F}_{\text{TTD},n}\big)\mathbf{F}_{\text{BB},n}\mathbf{s}_n + \mathbf{n}_n, \tag{50}$$

where $\mathbf{F}_{\text{TTD},n} \in \mathbb{C}^{M\times N_{\text{RF}}}$ and $[\mathbf{F}_{\text{TTD},n}]_{m,l}$ denotes the phase shift introduced by the TTD lines at the mth phase shifter connected to the lth RF chain. Denoting

$$\mathbf{\Psi}_n \triangleq \begin{bmatrix} e^{-j2\pi(n-1)\eta t_{1,1}} & \dots & e^{-j2\pi(n-1)\eta t_{N_{\text{RF}},1}} \\ e^{-j2\pi(n-1)\eta t_{1,2}} & \dots & e^{-j2\pi(n-1)\eta t_{N_{\text{RF}},2}} \\ \vdots & \ddots & \vdots \\ e^{-j2\pi(n-1)\eta t_{1,V_{TTD}}} & \dots & e^{-j2\pi(n-1)\eta t_{N_{\text{RF}},V_{TTD}}} \end{bmatrix} \in \mathbb{C}^{V_{TTD}\times N_{\text{RF}}}, \tag{51}$$

$\mathbf{F}_{\text{TTD},n}$ can be expressed as

$$\mathbf{F}_{\text{TTD},n} = \mathbf{\Psi}_n \otimes \mathbf{1}_{M_T\times 1}. \tag{52}$$

Denote the equivalent analog beamforming matrix as $\tilde{\mathbf{F}}_{\text{RF},n} = \mathbf{F}_{\text{RF}} \odot (\mathbf{\Psi}_n \otimes \mathbf{1}_{M_T\times 1})$. Then, (50) can be simplified as

$$\mathbf{y}_n = \mathbf{H}^H\tilde{\mathbf{F}}_{\text{RF},n}\mathbf{F}_{\text{BB},n}\mathbf{s}_n + \mathbf{n}_n, \tag{53}$$

where the analog beamformer $\tilde{\mathbf{F}}_{\text{RF},n}$ can generate the frequency-dependent phase shifts and suffice for wideband beamforming.

Similar to Section IV-D, the hybrid precoding algorithm with the help of TTD lines can be summarized as follows:

- **Step 1: Input** $\mathbf{H}_n$ in (10) and the corresponding channel parameters ψ_l, τ_l and α_l.
- **Step 2:** Arrange the channel parameters subject to $\alpha_1 \geq \alpha_2 \geq \cdots \geq \alpha_L$.
- **Step 3:** For each $l \in \{1,\dots,N_{\text{RF}}\}$[4], in terms of (44), calculate $t_{l,v} = (v-1)M_T\frac{\psi_l}{f_c}$ and $\phi_{l,v} = -\pi(v-1)M_T\psi_l\frac{W}{f_c}$.
- **Step 4:** Build $\mathbf{F}_{\text{RF}}$ as

$$[\mathbf{F}_{\text{RF}}]_{:,l} = \frac{1}{\sqrt{M}}\Big[1,\dots,e^{-j2\pi(m-1)(\psi_l+\psi_l\frac{W}{2f_c})}e^{-j\phi_{l,\lceil\frac{m}{M_T}\rceil}},\dots,e^{-j2\pi(M-1)(\psi_l+\psi_l\frac{W}{2f_c})}e^{-j\phi_{l,V_{TTD}}}\Big]^T.$$

- **Step 5:** Determine $\mathbf{\Psi}_n$ according to (51) and $\tilde{\mathbf{F}}_{\text{RF},n} = \mathbf{F}_{\text{RF}} \odot (\mathbf{\Psi}_n \otimes \mathbf{1}_{M_T\times 1})$.
- **Step 6:** Calculate $\tilde{\mathbf{H}}_n = \mathbf{H}_n^H\tilde{\mathbf{F}}_{\text{RF},n}\big(\tilde{\mathbf{F}}_{\text{RF},n}^H\tilde{\mathbf{F}}_{\text{RF},n}\big)^{-\frac{1}{2}}$ and obtain its SVD as $\tilde{\mathbf{H}}_n = \tilde{\mathbf{U}}_n\tilde{\mathbf{\Sigma}}_n\tilde{\mathbf{V}}_n^H$.
- **Step 6:** Build $\mathbf{F}_{\text{BB},n} = \big(\tilde{\mathbf{F}}_{\text{RF},n}^H\tilde{\mathbf{F}}_{\text{RF},n}\big)^{-\frac{1}{2}}[\tilde{\mathbf{V}}_n]_{:,1:N_S}$.
- **Step 7: Output** $\mathbf{F}_{\text{RF}}$ in Step 4, $\mathbf{F}_{\text{BB},n}$ in Step 6, and $t_{l,v}$ in Step 3 as the delay set for the vth TTD line connected to the lth RF chain.

[4]When $L > N_{\text{RF}}$, one or several paths with smallest complex gains will be ignored. When $L < N_{\text{RF}}$, we can simply assume that $\alpha_{L+1} = \cdots = \alpha_{N_{\text{RF}}} = 0$.

D. Insertion Loss of the Proposed Architectures

Different from the baseband digital processing, the analog signal processing in RF components generally introduces the insertion loss [2], i.e., the RF signal power will reduce when passing through an analog component, which becomes severe in the THz frequency band. Since the proposed hybrid beamforming approach in this section employs the TTD lines, the additional insertion loss caused by the TTD lines will be introduced simultaneously.

Denote P_{init} as the total initial transmit power. For the virtual sub-array based beam broadening design in Section IV, since the hardware architecture does not alter compared with the conventional fully-connected hybrid architecture, the insertion loss of it remains the same and can be expressed as [38]

$$P_{\text{sub}} = P_{\text{init}} - L_{SP} - L_{PS} - L_{CB} + G_{PA}, \tag{54}$$

where $L_{SP} = 10\log_{10}M$ is the insertion loss of a splitter between an RF chain and the phase shifters, L_{PS} is the associated insertion loss of the phase shifters, $L_{CB} = 10\log_{10}N_{\text{RF}}$ is the insertion loss of the combiner between the phase shifters and the power amplifier (PA, next to the transmit antennas), and G_{PA} denotes the power gain of a PA. For the TTD-based analog beamformer design in this section, considering the insertion loss of TTD lines, the remained power at the transmit antennas is given by

$$P_{\text{TTD}} = P_{\text{init}} - L_{SP,TTD} - L_{TTD} - L_{SP,PS} - L_{PS} - L_{CB} + G_{PA}, \tag{55}$$

where $L_{SP,TTD} = 10\log_{10}V_{TTD}$ is the insertion loss of the additional splitter next to a TTD line, L_{TTD} is the insertion loss of TTD lines, and $L_{SP,PS} = 10\log_{10}M_T$ is the insertion loss of the combiner between the phase shifters and the PA.

As $P_{\text{TTD}} - P_{\text{sub}} = -L_{TTD}$, the TTD-based hybrid architecture induces the additional insertion loss caused exclusively by the TTD lines. However, such insertion loss does not impact the beamforming gain discussed before this subsection of this paper. Actually, it can be simply eliminated by introducing the extra PAs to compensate the insertion loss.

VI. Simulations

In this section, we present the numerical results to demonstrate the effectiveness of two proposed wideband beamforming approaches for hybrid transceivers. The BS and the served user are equipped with $M = 512$ antennas and $M_U = 32$ antennas, respectively. The antenna spacing for each ULA is $\frac{\lambda_c}{2}$. The carrier frequency and the bandwidth are set as $f_c = 300$ GHz and $W = 15$ GHz, respectively, where the number of subcarriers for the OFDM system is $N = 256$. The length of CP is $N_{\text{CP}} = 32$. The path delay is uniformly

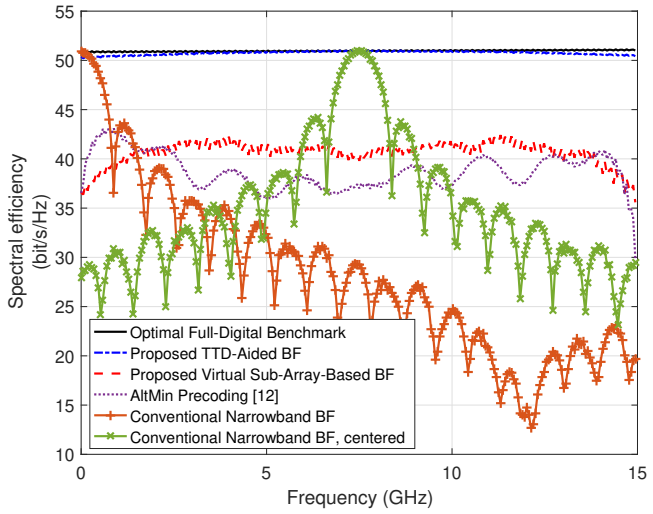

Fig. 8. Spectral efficiency across the whole frequency band in a four-path channel.

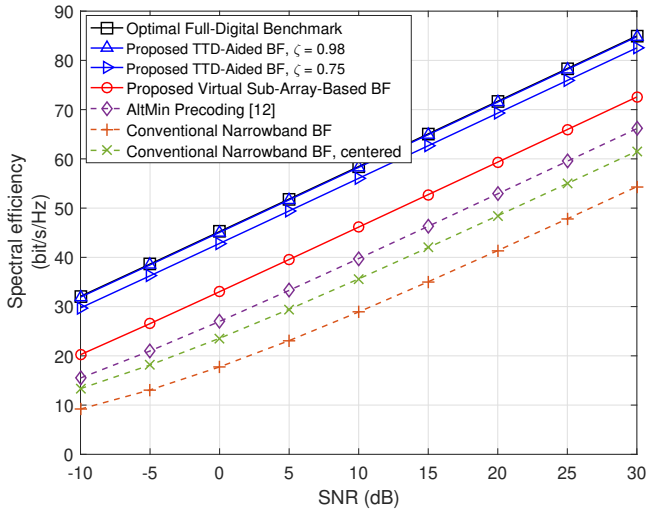

Fig. 9. Average spectral efficiency versus SNR.

drawn from $0 \sim 1$ ns [39], [40]. The number of RF chains and that of data streams are set as $N_S = N_{\text{RF}} = 4$. The downlink THz channel is assumed to contain one line-of-sight (LoS) path and $1 \sim 5$ non-LoS multipath components while the non-LoS paths have $-5 \sim -10$ dB power loss compared to the LoS one. Considering the worst case that the maximum path angle is $\max_l\{\psi_l\} = \pm\frac{\pi}{2}$ and requiring $\zeta = 0.98$ such that the average array gain is at least $0.98\sqrt{M}$, we choose $V_{TTD} = 34$ and $M_T = 15$ in terms of (47) for the TTD-aided approach.

We first show an example of the spectral efficiency across different frequencies in a four-path channel by different kinds of hybrid beamforming and precoding approaches, as shown in Fig. 8. In this example, the SNR is 10 dB. The optimal full-digital precoding is provided as a benchmark, which provides the evenly-distributed and the highest spectral efficiency over the whole bandwidth. The proposed TTD-aided approach gives the performance pretty close to the optimal full-digital precoding thanks to the delay compensation by the TTD lines. Due to the neglect of beam squint, the conventional narrowband beamforming techniques, which adopt steering vector $\mathbf{a}(\psi_l)$ or $\mathbf{a}(1.025\psi_l)$ as the beamforming vector for each path, only performs well at a small frequency range within the whole bandwidth. The wideband precoding algorithm based on the alternating minimization optimization (AltMin) in [12] is also provided for comparison. Without the TTD lines, the virtual sub-array based approach gives the approximately evenly-distributed but lower spectral efficiency compared with the TTD-aided approach.

Fig. 9 shows the average spectral efficiency (ASE) over the whole bandwidth by different kinds of hybrid beamforming and precoding approaches. The ASE of the proposed TTD-aided approach with $\zeta = 0.98$ performs nearly the same as the full-digital precoding. In addition, the ASE of the proposed TTD-aided approach with $\zeta = 0.75$ is also presented, where only $V_{TTD} = 9$ TTD lines are needed for each RF chains

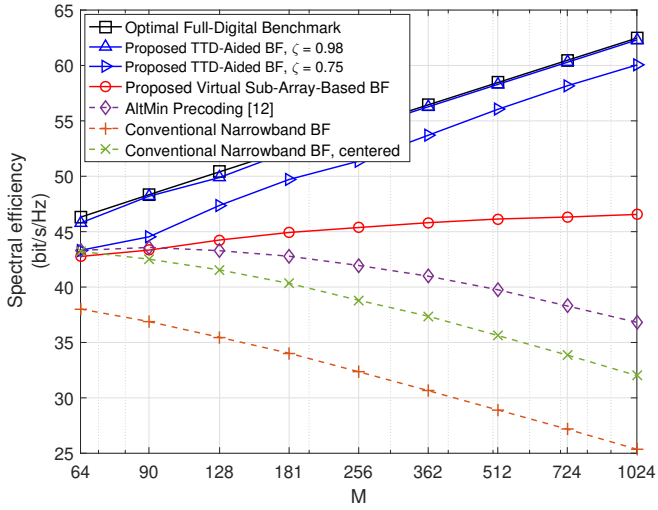

Fig. 10. Average spectral efficiency versus the number of BS antennas.

and the number of antennas connected to each TTD line is $M_T = 54$. In this case, although the average array gain is just 75% of that in the full-digital precoding, the TTD-aided approach still provides a decent performance, with a small gap compared to the ASE of the full-digital precoding. In this figure, the virtual sub-array based approach achieves the lower ASE but still outperforms the other algorithms such as AltMin [12] which uses the iterative optimization to determine the phase shifts. Note that without the delay compensation provided by TTD lines, there naturally exists the incompatibility between the requirement of mitigating the beam squint effect and the hardware implementation of analog beamformer in phased array transceivers, which largely limits of performance of wideband beamforming.

Fig. 10 presents the ASE under different numbers of the BS antennas while the other system parameters are set the same as in the first paragraph of this section. The TTD-aided ap-

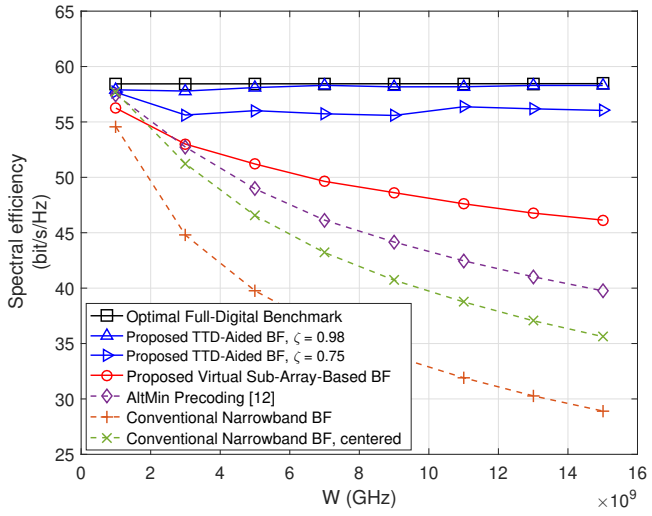

Fig. 11. Average spectral efficiency versus the transmission bandwidth.

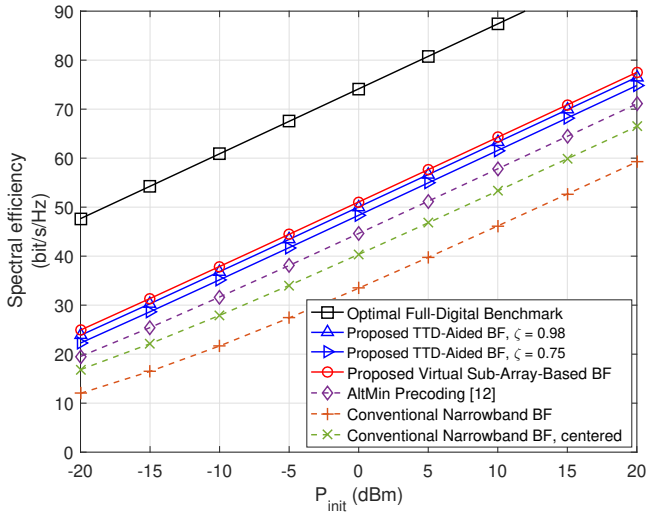

Fig. 13. Average spectral efficiency versus initial transmit power in dBm.

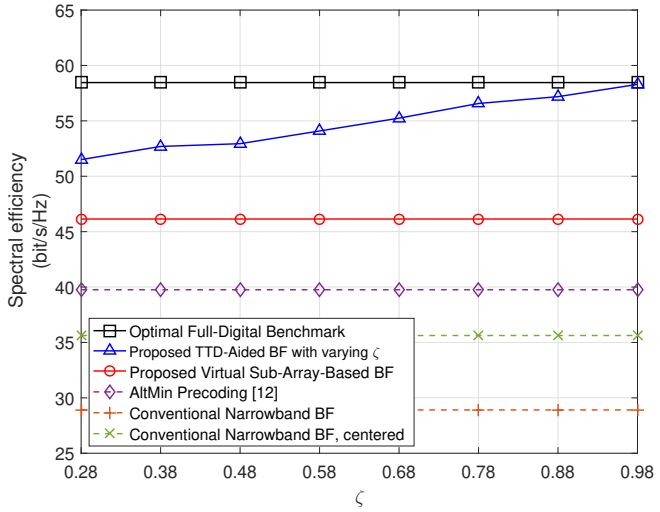

Fig. 12. Average spectral efficiency versus ζ.

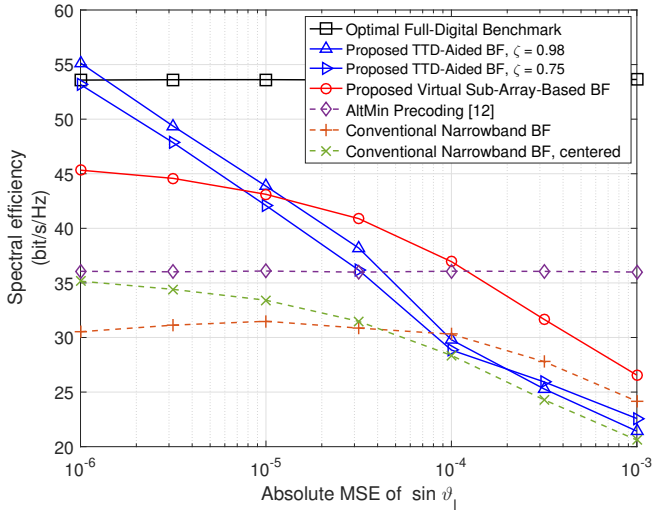

Fig. 14. Average spectral efficiency versus estimation error of path angles.

proach can provide the near-optimal results with larger ζ. The proposed virtual sub-array based approach gives the decent performance with the increase of M, which demonstrates that the beam broadening technique in Section IV can partially tackle the beam squint issue even without the help of TTD lines. Fig. 11 shows the ASE under different bandwidths while the other system parameters are set the same as in the first paragraph of this section. With the increase of the transmission bandwidth, the performance gap between the proposed TTD-based approach and the non-TTD-based ones becomes larger, which indicates the necessity of settling the incompatibility between beam squint and analog hardware implementation of hybrid phased arrays in the scenarios with large bandwidth and large numbers of antennas.

Fig. 12 depicts the relationship between the number of TTD lines and ASEs. Except for ζ, other parameters are set the same as the previous simulation. Since ζ and M_T are linked by equation (47), a larger ζ results in a smaller M_T and thus a larger V_{TTD}, and has better performance according to (46) and (49). In this figure, $\zeta = 0.28$ corresponds to $V_{TTD} = 5$ and $\zeta = 0.98$ corresponds to $V_{TTD} = 34$.

Fig. 13 shows the ASE over the whole bandwidth with consideration of the insertion loss discussed in Section V-D, where $L_{TTD} = 10$ dB [35], [41], $L_{PS} = 5$ dB [38], $G_{PA} = 30$ dB [42], [43], and the noise power is set as -70 dBm. Due to the insertion loss, the TTD-based hybrid structure is confronted with the lower ASE at the same initial transmit power. Nevertheless, since the insertion loss happens in the RF circuits before the transmit antennas, it has no impact on the beamforming gain and can be readily alleviated by employing the extra PAs associated as the TTD lines.

While the above numerical results are based on the accurate channel and AoA information, Fig. 14 illustrates the impact of channel estimation error on the precoding performance.

In this figure, the normalized mean-squared error (MSE) of the complex gain of channel paths is assumed 10^{-1} and the absolute MSE of $\sin\vartheta_l$ varies from 10^{-6} to 10^{-3}. The case of more TTD lines will be more sensitive to the estimation error of path angles. Hence, $\zeta = 0.98$ performs better than $\zeta = 0.75$ with low absolute MSE of $\sin\vartheta_l$ but performs worse than $\zeta = 0.75$ with high absolute MSE of $\sin\vartheta_l$. Due to large beam width, the virtual sub-array based approach is more robust to the estimation error. Since the full-digital benchmark and the AltMin precoding directly use the whole channel matrix and do not employ the path angle information to determine the precoding matrix, their performance is independent of the estimation error of the path angles.

VII. Conclusions

In this paper, we have proposed two wideband beamforming approaches for hybrid transceivers to eliminate the impact of beam squint. If we keep the current fully-connected hybrid architecture, the virtual sub-array based approach can be used to combat beam squint. The virtual sub-array realizes the beam broadening in analog beamforming, which provides the evenly distributed array gain across the whole operating frequency band and partially alleviate the impact of beam squint. However, the virtual sub-array does not address the incompatibility between the requirement of mitigating beam squint and the narrowband feature of phase shifters. To fully enable the wideband beamforming ability for an analog beamformer, we redesign the analog beamformer and propose a TTD-aided approach. The TTD-aided approach largely alleviates the incompatibility and thus achieves the near-optimal performance close to the full-digital transceivers but meanwhile has higher hardware cost and larger power consumption. Analytical and numerical results demonstrate the effectiveness of two proposed wideband beamforming techniques and the necessity of full consideration of beam squint under hybrid massive MIMO THz communications.

Appendix A

In terms of (29), when $x \neq 0$, the array gain can be written as

$$\begin{aligned}
|\mathbf{a}^H(\Xi_l(f))\mathbf{g}_l| &= \left| \sum_{v'=1}^{V}\sum_{m=1}^{M_s} \frac{1}{\sqrt{VM_s}} e^{-j2\pi[(v'-1)M_s+(m-1)]\tilde{\psi}_{l,v'}} \right. \\
&\qquad \left. \times\, e^{-j\phi_{l,v'}} e^{j2\pi[(v'-1)M_s+(m-1)]\Xi_l(f)} \right| \\
&= \left| \frac{1}{\sqrt{VM_s}} \sum_{v'=1}^{V}\sum_{m=1}^{M_s} e^{-j2\pi[(v'-1)M_s+(m-1)](\psi_l+\frac{2v'-1}{2M_s})} e^{-j\pi\frac{v'-1}{M_s}} \right. \\
&\qquad \left. \times\, e^{j2\pi[(v'-1)M_s+(m-1)](\psi_l+\frac{v_f}{M_s}+\frac{x}{M_s}-\frac{1}{2M_s})} \right| \\
&= \left| \frac{1}{\sqrt{VM_s}} \sum_{v'=1}^{V}\sum_{m=1}^{M_s} e^{-j2\pi[(v'-1)M_s+(m-1)]\frac{v'-v_f-x}{M_s}} e^{-j\pi\frac{v'-1}{M_s}} \right| \\
&= \left| \frac{1}{\sqrt{VM_s}} \sum_{v'=1}^{V} e^{-j2\pi(v'-1)(v'-v_f-x)} e^{-j\pi\frac{v'-1}{M_s}} \right. \\
&\qquad \left. \times \sum_{m=1}^{M_s} e^{-j2\pi\frac{m-1}{M_s}(v'-v_f-x)} \right|. \qquad (56)
\end{aligned}$$

When $x \in (0, \frac{1}{2})$, likewise, we only need to consider the items satisfying $v' = v_f$ and $v' = v_f + 1$ in the summation of (56), which can be determined as

$$\begin{aligned}
&|\mathbf{a}^H(\Xi_l(f))\mathbf{g}_l| \\
&= \frac{1}{\sqrt{VM_s}} \left| e^{j2\pi(v-1)x} e^{-j\pi\frac{v-1}{M_s}} \sum_{m=1}^{M_s} e^{j2\pi\frac{m-1}{M_s}x} \right. \\
&\qquad \left. + e^{j2\pi v(x-1)} e^{-j\pi\frac{v}{M_s}} \sum_{m=1}^{M_s} e^{-j2\pi\frac{m-1}{M_s}(1-x)} \right| \\
&= \frac{1}{\sqrt{VM_s}} \left| e^{-j2\pi x} e^{j\pi\frac{1}{M_s}} \frac{\sin(\pi x)}{\sin(\pi x/M_s)} e^{j\pi(M_s-1)\frac{x}{M_s}} \right. \\
&\qquad \left. + \frac{\sin(\pi(1-x))}{\sin(\pi(1-x)/M_s)} e^{-j\pi(M_s-1)\frac{1-x}{M_s}} \right| \\
&= \frac{1}{\sqrt{VM_s}} \left| e^{-j2\pi x} \frac{\sin(\pi x)}{\sin(\pi x/M_s)} - \frac{\sin(\pi x)}{\sin(\pi(1-x)/M_s)} \right| \\
&\approx \sqrt{\frac{M_s}{V}} \sin(\pi x) \left| e^{-j2\pi x} \frac{1}{\pi x} - \frac{1}{\pi(1-x)} \right| \\
&= \sqrt{\frac{M_s}{V}} \sin(\pi x) \sqrt{\frac{1}{\pi^2 x^2} - \frac{2\cos(2\pi x)}{\pi^2 x(1-x)} + \frac{1}{\pi^2(1-x)^2}}. \qquad (57)
\end{aligned}$$

By the same manipulation, when $x \in (-\frac{1}{2}, 0)$, only items satisfying $v' = v_f - 1$ and $v' = v_f$ in the summation of (56) need to be considered such that

$$\begin{aligned}
&|\mathbf{a}^H(\Xi_l(f))\mathbf{g}_l| \\
&= \frac{1}{\sqrt{VM_s}} \left| e^{j2\pi x} \frac{\sin(\pi x)}{\sin(\pi x/M_s)} - \frac{\sin(\pi(x+1))}{\sin(\pi(x+1)/M_s)} \right| \\
&\approx \sqrt{\frac{M_s}{V}} (-\sin(\pi x)) \left| e^{j2\pi x} \frac{1}{\pi x} + \frac{1}{\pi(x+1)} \right| \\
&= \sqrt{\frac{M_s}{V}} (-\sin(\pi x)) \sqrt{\frac{1}{\pi^2 x^2} + \frac{2\cos(2\pi x)}{\pi^2 x(x+1)} + \frac{1}{\pi^2(x+1)^2}}. \qquad (58)
\end{aligned}$$

References

[1] H. Sarieddeen, N. Saeed, T. Y. Al-Naffouri, and M. Alouini, "Next generation terahertz communications: A rendezvous of sensing, imaging, and localization," *IEEE Commun. Mag.*, vol. 58, no. 5, pp. 69–75, May 2020.

[2] C. Lin and G. Y. Li, "Terahertz communications: An array-of-subarrays solution," *IEEE Commun. Mag.*, vol. 54, no. 12, pp. 124–131, Dec. 2016.

[3] C. Lin, G. Y. Li, and L. Wang, "Subarray-based coordinated beamforming training for mmWave and sub-THz communications," *IEEE J. Sel. Areas Commun.*, vol. 35, no. 9, pp. 2115–2126, Sep. 2017.

[4] ITU Publications, "World Radiocommunication Conference 2019 (WRC-19): Provisional Final Acts", Sharm el-Sheikh, Egypt, Oct. 2019.

[5] I. F. Akyildiz, C. Han, and S. Nie, "Combating the distance problem in the millimeter wave and terahertz frequency bands," *IEEE Commun. Mag.*, vol. 56, no. 6, pp. 102–108, Jun. 2018.

[6] I. F. Akyildiz and J. M. Jornet, "Realizing ultra - massive MIMO (1024x1024) communication in the (0.06 - 10) terahertz band," *Nano Commun. Networks*, vol. 8, pp. 46–54, Jun. 2016.

[7] C. Han, J. M. Jornet, and I. Akyildiz, "Ultra-massive MIMO channel modeling for graphene-enabled terahertz-band communications," *2018 IEEE 87th Veh. Technol. Conf. (VTC Spring)*, Porto, 2018.

[8] E. Bjornson, L. Van der Perre, S. Buzzi, and E. G. Larsson, "Massive MIMO in sub-6 GHz and mmWave: Physical, practical, and use-case differences," *IEEE Wireless Commun.*, vol. 26, no. 2, pp. 100–108, Apr. 2019.

[9] A. F. Molisch et al., "Hybrid beamforming for massive MIMO: A survey," *IEEE Commun. Mag.*, vol. 55, no. 9, pp. 134–141, Sep. 2017.

[10] J. Du, W. Xu, H. Shen, X. Dong, and C. Zhao, "Hybrid precoding architecture for massive multiuser MIMO with dissipation: Sub-connected or fully connected structures?", *IEEE Trans. Wireless Commun.*, vol. 17, no. 8, pp. 5465–5479, Aug. 2018.

[11] L. Liang, W. Xu, and X. Dong, "Low-complexity hybrid precoding in massive multiuser MIMO systems," *IEEE Wireless Commun. Lett.*, vol. 3, no. 6, pp. 653–656, Dec. 2014.

[12] X. Yu, J. Shen, J. Zhang, and K. B. Letaief, " "Alternating minimization algorithms for hybrid precoding in millimeter wave MIMO systems," *IEEE J. Sel. Topics Signal Process.*, vol. 10, no. 3, pp. 485–500, Apr. 2016.

[13] A. Garcia-Rodriguez, V. Venkateswaran, P. Rulikowski and C. Masouros, "Hybrid analog–digital precoding revisited under realistic RF modeling," *IEEE Wireless Commun. Lett.*, vol. 5, no. 5, pp. 528-531, Oct. 2016.

[14] S. A. Hoseini, M. Ding, and M. Hassan, "Massive MIMO performance comparison of beamforming and multiplexing in the terahertz band," *2017 IEEE Globecom Workshops (GC Wkshps)*, Singapore, 2017, pp. 1-6.

[15] G. Zhu, K. Huang, V. K. N. Lau, B. Xia, X. Li, and S. Zhang, "Hybrid beamforming via the Kronecker decomposition for the millimeter-wave massive MIMO systems," *IEEE J. Sel. Areas Commun.*, vol. 35, no. 9, pp. 2097–2114, Sep. 2017.

[16] F. Sohrabi and W. Yu, "Hybrid digital and analog beamforming design for large-scale antenna arrays," *IEEE J. Sel. Topics Signal Process.*, vol. 10, no. 3, pp. 501-513, Apr. 2016.

[17] T. E. Bogale, L. B. Le, and X. Wang, "Hybrid analog-digital channel estimation and beamforming: Training-throughput tradeoff," *IEEE Trans. Commun.*, vol. 63, no. 12, pp. 5235-5249, Dec. 2015.

[18] J. Chen, "Hybrid beamforming with discrete phase shifters for millimeter-wave massive MIMO systems," *IEEE Tran. Veh. Technol.*, vol. 66, no. 8, pp. 7604–7608, Aug. 2017.

[19] W. Ni, X. Dong, and W. Lu, "Near-optimal hybrid processing for massive MIMO systems via matrix decomposition," *IEEE Trans. Signal Process.*, vol. 65, no. 15, pp. 3922-3933, 1 Aug. 2017.

[20] L. Kong, S. Han, and C. Yang, "Hybrid precoding with rate and coverage constraints for wideband massive MIMO systems," *IEEE Trans. Wireless Commun.*, vol. 17, no. 7, pp. 4634-4647, Jul. 2018.

[21] W. Huang, Y. Huang, R. Zhao, S. He and L. Yang, "Wideband millimeter wave communication: Single carrier based hybrid precoding with sparse optimization," *IEEE Tran. Veh. Technol.*, vol. 67, no. 10, pp. 9696-9710, Oct. 2018.

[22] H. Yuan, N. Yang, K. Yang, C. Han, and J. An, "Hybrid beamforming for MIMO-OFDM terahertz wireless systems over frequency selective channels," *2018 IEEE Global Communications Conference (GLOBECOM)*, Abu Dhabi, United Arab Emirates, 2018.

[23] C. Lin and G. Y. Li, "Adaptive beamforming with resource allocation for distance-aware multi-user indoor terahertz communications," *IEEE Trans. Commun.*, vol. 63, no. 8, pp. 2985-2995, Aug. 2015.

[24] B. Wang, M. Jian, F. Gao, G. Y. Li, and H. Lin, "Beam squint and channel estimation for wideband mmwave massive MIMO-OFDM systems," *IEEE Trans. Signal Process.*, vol. 67, no. 23, pp. 5893–5908, Dec. 2019.

[25] B. Wang, F. Gao, S. Jin, H. Lin, and G. Y. Li, "Spatial- and frequency-wideband effects in millimeter-wave massive MIMO systems," *IEEE Trans. Signal Process.*, vol. 66, no. 13, pp. 3393–3406, Jul. 2018.

[26] B. Wang, F. Gao, S. Jin, H. Lin, G. Y. Li, S. Sun, and T. S. Rappaport, "Spatial-wideband effect in massive MIMO with application in mmWave systems," *IEEE Commun. Mag.*, vol. 56, no. 12, pp. 134–141, Dec. 2018.

[27] E. Vlachos, G. C. Alexandropoulos, and J. Thompson, "Wideband MIMO channel estimation for hybrid beamforming millimeter wave systems via random spatial sampling," *IEEE J. Sel. Topics Signal Process.*, vol. 13, no. 5, pp. 1136-1150, Sep. 2019.

[28] H. Li, M. Li, Q. Liu, and A. L. Swindlehurst, "Dynamic hybrid beamforming with low-resolution PSs for wideband mmWave MIMO-OFDM systems," *IEEE J. Sel. Areas Commun.*, vol. 38, no. 9, pp. 2168–2181, Sep. 2020.

[29] D. B. Hunter, M. E. Parker, and J. L. Dexter, "Demonstration of a continuously variable true-time delay beamformer using a multichannel chirped fiber grating," *IEEE Trans. Microwave Theory Technol*, vol. 54, no. 2, pp. 861–867, Feb. 2006.

[30] F. Zhang, J. Dong, Y. Zhu, X. Gao, and X. Zhang, "Integrated optical true time delay network based on grating-assisted contradirectional couplers for phased array antennas," *IEEE J. Sel. Topics Quantum Electro.*, vol. 26, no. 5, pp. 1–7, Sep.–Oct. 2020.

[31] L. Du, P. Yu, S. Hu, and H. Zhu, "Design of true time delay circuit based on thin-film coplanar waveguide," *2016 IEEE International Conference on Microwave and Millimeter Wave Technology (ICMMT)*, Beijing, 2016, pp. 120–122.

[32] R. Rotman, M. Tur, and L. Yaron, "True time delay in phased arrays," *Proceedings of the IEEE*, vol. 104, no. 3, pp. 504–518, Mar. 2016.

[33] M. Schartel, W. Mayer, and C. Waldschmidt, "Digital true time delay for pulse correlation radars," *2016 European Radar Conference (EuRAD)*, London, 2016, pp. 330–333.

[34] E. Carrasco, J. A. Encinar, and M. Barba, "Bandwidth improvement in large reflectarrays by using true-time delay," *IEEE Trans. Antennas Propag.*, vol. 56, no. 8, pp. 2496–2503, Aug. 2008.

[35] M. Longbrake, "True time-delay beamsteering for radar," *2012 IEEE National Aerospace and Electronics Conference (NAECON)*, Dayton, OH, 2012, pp. 246-249.

[36] D. Tse and P. Viswanath, *Fundamentals of Wireless Communication.* Cambridge, U.K.: Cambridge Univ. Press, 2004.

[37] H. L. Van Trees, *Optimum Array Processing (Detection, Estimation, and Modulation Theory, Part IV)*, John Wiley & Sons, Inc., 2002.

[38] C. Lin and G. Y. Li, "Energy-Efficient Design of Indoor mmWave and Sub-THz Systems With Antenna Arrays," *IEEE Trans. Wireless Commun.*, vol. 15, no. 7, pp. 4660–4672, Jul. 2016.

[39] C. Han, A. O. Bicen, and I. F. Akyildiz, "Multi-Ray channel modeling and wideband characterization for wireless communications in the terahertz band," *IEEE Trans. Wireless Commun.*, vol. 14, no. 5, pp. 2402–2412, May. 2015.

[40] K. Tsujimura, K. Umebayashi, J. Kokkoniemi, J. Lehtomäki, and Y. Suzuki, "A causal channel model for the terahertz band," *IEEE Trans. Terahertz Sci. Technol.*, vol. 8, no. 1, pp. 52–62, Jan. 2018.

[41] R. L. Q. Li, Zhenhai Fu, and R. Chen, "High packing density 2.5 THz true-time-delay lines using spatially multiplexed substrate guided waves in conjunction with volume holograms on a single substrate," *Journal of Lightwave Technol.*, vol. 15, no. 12, pp. 2253–2258, Dec. 1997.

[42] M. A. Basten, J. C. Tucek, D. A. Gallagher, K. E. Kreischer, and R. Mihailovich, "A 0.85 THz vacuum-based power amplifier," *IVEC 2012*, Monterey, CA, 2012, pp. 39–40.

[43] N. Deferm and P. Reynaert, *CMOS Front Ends for Millimeter Wave Wireless Communication Systems*. New York, NY, USA: Springer, 2015.

Feifei Gao (M'09–SM'14) received the B.Eng. degree from Xi'an Jiaotong University, Xi'an, China, in 2002, the M.Sc. degree from McMaster University, Hamilton, ON, Canada, in 2004, and the Ph.D. degree from National University of Singapore, Singapore, in 2007. He was a Research Fellow with the Institute for Infocomm Research (I2R), A*STAR, Singapore, in 2008 and an Assistant Professor with the School of Engineering and Science, Jacobs University, Bremen, Germany, from 2009 to 2010. In 2011, he joined the Department of Automation, Tsinghua University, Beijing, China, where he is currently an Associate Professor.

Prof. Gao's research areas include communication theory, signal processing for communications, array signal processing, and convex optimizations, with particular interests in MIMO techniques, multi-carrier communications, cooperative communication, and cognitive radio networks. He has authored/ coauthored more than 120 refereed IEEE journal papers and more than 120 IEEE conference proceeding papers, which have been cited more than 7000 times from Google Scholar. Prof. Gao has served as an Editor of IEEE Transactions on Wireless Communications, IEEE Transactions on Cognitive Communications and Networking, IEEE Signal Processing Letters, IEEE Communications Letters, IEEE Wireless Communications Letters, International Journal on Antennas and Propagations, and China Communications. He has also serves as the symposium co-chair for 2018 IEEE Vehicular Technology Conference Spring (VTC), 2015 IEEE Conference on Communications (ICC), 2014 IEEE Global Communications Conference (GLOBECOM), 2014 IEEE Vehicular Technology Conference Fall (VTC), as well as Technical Committee Members for many other IEEE conferences.

Bolei Wang (S'15–M'21) received the B.Eng. degree in electrical engineering from University of Electronic Science and Technology of China (UESTC), Chengdu, China, in 2015, and the Ph.D. degree from Tsinghua University, Beijing, China. His current research interests include signal processing for broadband wireless communications, with a focus on massive MIMO systems, millimeter-wave communications, and 5G New Radio. He was the recipient of a Best Paper Award in 2018 IEEE GLOBECOM and the Exemplary Reviewer of IEEE Communications Letters in 2018.

Geoffrey Ye Li (S'93–M'95–SM'97–F'06) has been a Chair Professor at Imperial College London, UK, since 2020. Before moving to Imperial, he was with Georgia Institute of Technology in Georgia, USA, as a Professor for twenty years and with AT&T Labs - Research in New Jersey, USA, as a Principal Technical Staff Member for five years. His general research interests include statistical signal processing and machine learning for wireless communications. In the related areas, he has published over 500 journal and conference papers in addition to over 40 granted patents. His publications have been cited over 45,000 times and he has been recognized as a Highly Cited Researcher, by Thomson Reuters, almost every year.

Dr. Geoffrey Ye Li was awarded IEEE Fellow for his contributions to signal processing for wireless communications in 2005. He won several prestigious awards from IEEE Signal Processing Society (Donald G. Fink Overview Paper Award in 2017), IEEE Vehicular Technology Society (James Evans Avant Garde Award in 2013 and Jack Neubauer Memorial Award in 2014), and IEEE Communications Society (Stephen O. Rice Prize Paper Award in 2013, Award for Advances in Communication in 2017, and Edwin Howard Armstrong Achievement Award in 2019). He also received the 2015 Distinguished ECE Faculty Achievement Award from Georgia Tech.

He has been involved in editorial activities for over 20 technical journals, including the founding Editor-in-Chief of IEEE JSAC Special Series on ML in Communications and Networking. He has organized and chaired many international conferences, including technical program vice-chair of the IEEE ICC'03, general co-chair of the IEEE GlobalSIP'14, the IEEE VTC'19 (Fall), and the IEEE SPAWC'20.